Atomic-scale observation of off-centering rattlers in filled skutterudites

Zhen-Hua Ge, Wen-Jie Li, Jing Feng, Fengshan Zheng, Chun-Lin Jia, Di Wu, and Lei Jin**

Z.-H. Ge, W.-J. Li, J. Feng
Faculty of Materials Science and Engineering, Kunming University of Science and Technology, Kunming 650093, Yunnan, China

F. Zheng, C.-L. Jia, L. Jin
Ernst Ruska-Centre for Microscopy and Spectroscopy with Electrons, Forschungszentrum Jülich GmbH, 52428 Jülich, Germany
E-mail: l.jin@fz-juelich.de

D. Wu
Key Laboratory for Macromolecular Science of Shaanxi Province, Shaanxi Key Laboratory for Advanced Energy Devices, School of Materials Science and Engineering, Shaanxi Normal University, Xi'an 710119, Shaanxi, China
E-mail: wud@snnu.edu.cn

Keywords: thermoelectrics, filled skutterudite, off-centering, rattle, negative spherical aberration imaging, electron microscopy

As one of the most fundamental order parameters, coordinate order of atoms is a cornerstone in determining the physical and chemical properties of materials. Off-centering shifts of atoms from their centrosymmetric positions, a phenomenon that is closely related to symmetry breaking and structural transitions in crystals, is of key importance to modify a broad range of fundamental properties, such as ferroelectricity, antiferroelectricity and piezoelectricity. In thermoelectric materials, which can be used to directly interconvert heat to electricity, off-centering was proposed in, *e.g*., lead tellurides, halide perovskites, type I and II clathrates and filled skutterudites, to be the physical origin of the experimentally-measured exceptionally low thermal conductivity, but only indirectly supported from structural refinements and experimental/theoretical vibration mode analyses. In this work, we take Yb partially-filled and Ce fully-filled skutterudite as a model system for directly measuring the off-centering shifts of filler atoms, *i.e*., rattlers, with picometer precision in real space, by means of atomic-

resolution negative spherical aberration imaging transmission electron microscopy. This finding allows an in-depth understanding of the relation between the off-centering and the thermoelectric performance, and the presented methodology here is also applicable to investigate the off-centering phenomena in other functional materials, *e.g.*, ferroelectrics and solar cells.

1. Introduction

Thermoelectric materials are the basis for devices that can directly convert heat to electricity and vice versa, thus holding promises to solve the growing energy crisis nowadays. The performance of a thermoelectric material is evaluated by a dimensionless figure of merit value, $ZT = \sigma S^2 T/\kappa$, where σ, S, T and κ are electrical conductivity, Seebeck efficiency, absolute temperature (in Kelvin) and thermal conductivity, respectively. An ideal thermoelectric material shall be simultaneously a decent charge conductor and a heat insulator, *i.e.*, phonon glass electron crystal (PGEC) as proposed by Slack.[1] Among all state-of-the-art material series explored so far, skutterudites are deemed as decent mid-temperature thermoelectric materials for their unique and regulable crystal structure.

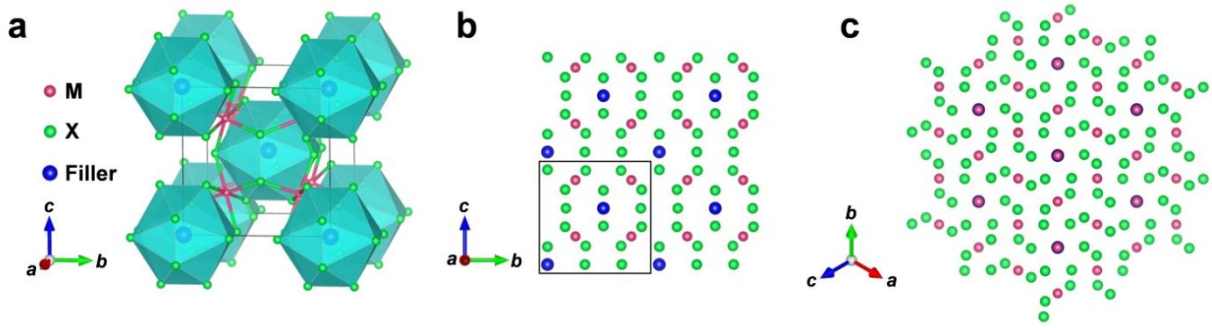

Figure 1. Schematics of the crystal structure of a filled skutterudite FM_4X_{12}. (a) Perspective of a unit cell. M atoms: green; X atoms: red; Filler atoms (F): blue. (b) Projection of 2×2×2 unit cells along the <100> axis. The filler atoms are isolated by the skutterudite framework atoms-M_4X_{12}. The selection of unit cell, marked by the black frame, is deliberately shifted away from the filler site as in (a) so that all atoms are fully included in the cell. (c) Projection of a filled skutterudite along the <111> direction. Note that the filler atoms align coincidently with M atoms in the viewing direction, resulting in intrinsic difficulties in quantitative characterization of filling atoms.

Skutterudite, characterized by the chemical formula MX_3 (M = Co, Rh or Ir and X = P, As or Sb), represents an extended group of materials that can be derived from the cobalt arsenide mineral $(Co,Fe,Ni)As_3$ discovered in 1845.[2] Under ambient conditions, skutterudite exhibits a high-symmetrical cubic structure (space group: $Im\bar{3}$, No. 204) with intrinsic inner "cages" formed by corner-sharing MX_6 octahedra, in which a variety of guest atoms can be filled.[2] The atoms in the cages are thus termed as fillers. Figure 1a shows the crystal structure of a filled skutterudite in the depiction using 8 × MX_6 corner-sharing octahedra (see the red-and-green ball-and-stick model) in a unit cell as well as the cage-like structure formed by filler-Sb_{12} icosahedra (see cyan cages). In this unit cell, atoms M and X are located at the 8c and 24g Wyckoff positions, respectively, while the filler (F) occupies the 2a position, *i.e.*, the apex and body center of the unit cell lattice. It is therefore common in literature to describe skutterudite as the half of the unit cell, FM_4X_{12}.[2]

The most studied skutterudites for mid-temperature thermoelectric applications are antimony-based alloys, *i.e.*, $(Fe,Co)_4Sb_{12}$, due to the relatively high power factor (σS^2) and comparatively low thermal conductivity that could be achieved deliberately through structural modifications.[3-6] The most effective structural modification in $(Fe,Co)_4Sb_{12}$ is to introduce fillers into the interstitial sites of the cage-like $(Fe,Co)_4Sb_{12}$ lattice. The fillers are usually foreign atoms, for instance, alkali metals,[7,8] rare earth,[9-12] alkaline earth,[13-15] and the XIII group elements,[16-19] which are believed to enhance phonon scattering and thus lower the thermal conductivity.[2] It is generally accepted that this effect on the thermal transport is attributed to the interaction between heat-carrying phonons and "rattling" fillers. In this regard, filler atoms are assumed to be loosely bonded with surrounding (Fe,Co)-Sb "cages" and thus rattling around individual equilibrium positions with one or more characteristic frequencies (thus called rattlers).[20-22] Hereby, filled skutterudites exhibit the synergetic characters of "rigid/stiff framework" and "glass-like vibrator", thus matching quite well with the concept of PGEC in thermoelectrics.[1]

However, the scenario that filler atoms rattle in the (Fe,Co)-Sb cages with fixed frequencies fails to explain the experimentally-measured exceptional low lattice thermal conductivity, as the nondispersive and localized resonant scattering of phonons by fillers only provides a rather limited impedance on the thermal transport. Off-centering of filler atoms was then proposed in skutterudites to explain this discrepancy, and its function could be intepreted as either of the two aspects as follows. In the aspect of lattice strain, off-centered fillers could

result in anisotropic distortion on surrounding icosahedral "cages"; while in the aspect of phonon spectrum, the off-center effect broadens the resonant frequency of rattlers thus leading to a flattened lattice vibration spectrum. Chakoumakos *et al.* reported in 1999 an anomalously large displacement of La off the "cage" center in $LaFe_3CoSb_{12}$ by structural refinement based on neutron diffraction experiments;[23] Goto *et al.* deduced a thermally activated off-center rattling of Pr ion in the cage of Sb-icosahedron in $PrOs_4Sb_{12}$ from experimental observations of an ultrasonic dispersion of elastic constants; using electron-spin-resonance technique;[24] Garcia *et al.* found the coexistence of on-center and off-center Yb^{3+} rattles in Ce/Yb double-filled FeP_3;[25] most recently, Fu *et al.* domonstrated Sn off-centers in its coordination cage, which leads to low-frequency Goldstone-like modes and accounts for the ultralow lattice thermal conductivity in $SnFe_4Sb_{12}$.[26]

In addition, extensive efforts have also been devoted to the detection of fillers in real space, *i.e.,* using advanced atomic-resolution transmission electron microscopy (TEM).[4,27-30] However, direct evidence of positions as well as concentration for filler atoms was rarely reported, in particular at the atomic resolution. Up to now, the widely-used technique for investigation of the off-center behavior of the fillers is high-angle annular dark-field (HAADF) scanning transmission electron microscopy (STEM), whose image contrast is approximately proportional to Z^2 (Z: atomic number).[31] It is thus commonly called Z-contrast imaging. Therefore, a major challenge for HAADF STEM imaging is that the contrast from filler atoms is typically weak, either below the detection sensitivity or far from being quantitative. This is not only due to the low Z nature of filler atoms, *e.g.*, Ga (Z = 31), but also due to the partial occupancy in the cage because of limited solubility.

For example, in <111> zone axes, as shown in Figure 1c, the filler atoms align coincidently with M (*e.g.*, Fe, Co) atoms, resulting in intrinsic difficulties in quantitative measurements of filling atoms (Supporting Information, Note 1). While in <100> zone axes, as shown in Figure 1b, the density of the isolated filler atoms (per projected atomic columns) is only half that of the neighboring X atoms (*e.g.*, Sb with Z = 51). The density is even lower given the partially-filled nature at the positions. These together lead to relatively weak contrast of the filler atoms so that they cannot be distinguished from the surrounding Sb in HAADF STEM imaging (Supporting Information, Note 2). Furthermore, the residual aberrations, scanning distortion, *etc*, are also non-trivial issues in quantification of the filler atoms. Therefore, techniques that can image the filler atoms with high spatial resolution and high image contrast are crucial to

understand the relation between the thermoelectric performance and the behavior of the filler atoms in skutterudites.

In this work, we present a detailed TEM study of both N-type and P-type filled $(Co,Fe)_4Sb_{12}$ thermoelectric alloys employing the negative spherical aberration imaging (NCSI) technique.[32] This technique provides high contrast of both light and heavy atoms and allows ultra-high precision measurement of atom positions.[33-35] We have observed the filler atoms of nominally 20 at.% Yb and fully-filled Ce in skutterudite $(Co,Fe)_4Sb_{12}$ and measured their off-center shifts cage-by-cage with picometer precision on the basis of quantitative high-resolution TEM (HRTEM). The influence of off-center shifts of rattling filler atoms on the thermoelectric properties is further evaluated based on a modified Debye-Callaway model. Our work for the first time provides direct evidence on the off-centering rattlers in skutterudites and may shed light on further evidencing off-center atoms in real space for a broad series of thermoelectric materials.

2. Results and discussion

2.1. Visualization of filler atoms using NCSI

Figure 2a-c shows the atomic-resolution TEM images recorded along the <001> crystal axis under the NCSI conditions for the unfilled Co_4Sb_{12} (pure), nominally 20 at.% Yb filled Co_4Sb_{12} (N-type) and 100 at.% Ce filled $(CoFe_3)Sb_{12}$ (P-type) samples, respectively. In striking contrast to HAADF STEM images (Supporting Information, Note 2), all atomic columns, including the low concentration filler Yb (and even Li, see Supporting Information, Note 3), are clearly resolved using NCSI (see, *e.g.*, Yb atom marked by the filled arrow in Figure 2b). The visualization is more pronounced from the unit-cell-averaged experimental images (marked by red frames) overlaid on the bottom right corner of Figure 2a-c, alongside the best-fit simulated images marked by green frames (See Supporting Information, Note 4 for more details). From the best-fit images, the concentration of filler atoms averaged over the region of measurement is also determined, which is approximately 17.5 at.% for Yb and 80 at.% for Ce. The deviation of Ce from its nominal filling stoichiometry indicates a limited solubility of Ce in skutterudites. Similar reduction in solubility has also been reported in $CeFe_4Sb_{12}$[36] and $Ce_{0.1}Co_4Sb_{12}$[37].

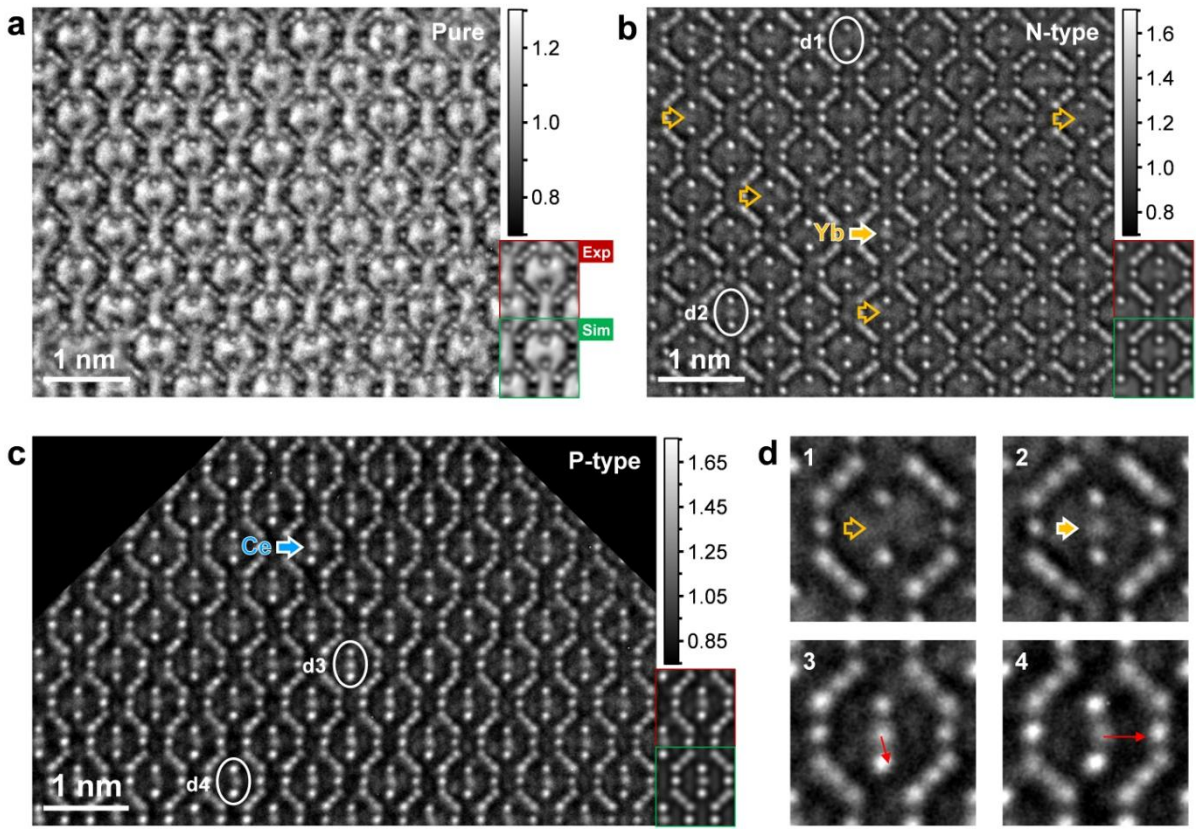

Figure 2. Atomic-resolution TEM images of (a) unfilled Co_4Sb_{12} (pure), (b) nominally 20 at.% Yb filled Co_4Sb_{12} (N-type) and (c) nominally 100 at.% Ce filled $(CoFe_3)Sb_{12}$ (P-type) samples along the <100> crystal axis. Images were recorded under the NCSI conditions. Unit-cell-averaged experimental images and correspondingly the best-fit simulated images are shown in the insets marked by red and green frames, respectively, on the bottom right corner. Images in (a) to (c) are displayed in the same grey scale. (d) Magnified images of individual cages, namely d1 to d4, marked by ellipses in (b) and (c), showing four representative configurations of the filler atoms.

This unique capability of the NCSI technique further allows different configurations of the filler atoms to be studied cage-by-cage in both N- and P-type samples. Four individual configurations of filler atoms, *i.e.*, d1 to d4 (white ellipses in Figure 2b and 2c) are displayed in Figure 2d as examples. Unlike the P-type sample that has relatively high filling rate (thus high and homogeneous Ce occupancy shown in Figure 2c), the N-type skutterudite shows local inhomogeneity in the filler's distribution, as directly evidenced by the presence of empty Yb sites (see, *e.g.*, d1 and those marked by open arrows in Figure 2b) with no evident contrast in comparison with those occupied positions indicated by filled arrows (*e.g.*, d2). This finding is consistent with the low filling ratio in the N-type sample.

Noticeably, the filler atoms are found not always to locate the centrosymmetric positions (*i.e.*, cage center) as illustrated in Figure 1a. Instead, they exhibit essential off-center shifts away from the centrosymmetric positions, *e.g.*, in cage d3 and d4, where the off-center shifts of the Ce atoms are marked by red arrows in Figure 2d. Such shifts turn out to be more prominent in the Ce-filled P-type sample, in comparison with the Yb-filled N-type skutterudite.

2.2. Quantitative measurements of off-center shifts

In order to quantify this off-centering phenomenon, the actual position of each individual intensity maximum in the original image is then determined by fitting two dimensional (2D) Gaussians to its intensity distribution.[38] After proper correction of the effect resulted from imaging imperfections (such as unavoidable sample mistilt from ideal Laue zone directions and residual lens aberrations; so-called imaging artifacts) using quantitative image simulations (Supporting Information, Note 4), the measured positions of the intensity maxima in the image represent the atomic positions in the material. Using these positions, the measurement error,[35] defined by the root mean square (rms) of atom-site deviations between the experimental and the best-fit periodic lattice of the Co_4Sb_{12} framework, is better than 7 pm in both horizontal (***x***) and vertical (***y***) directions for all samples used (see Supporting Information, Note 5). This measurement error, *i.e.*, precision of atom position measurement, serves as an important basis criterion for subsequent analyses of the filler atoms.

Figure 3 shows the results of off-center shifts in the P-type sample after correction for the known imaging artifacts. In Figure 3a, a larger specimen area is used in order to get better statistics. The off-center shifts of the Ce filler atoms are measured as the position deviation of Ce with respect to the calculated center of the two closest Sb neighbors (in the projected plane), as demonstrated in the inset to Figure 3a. In this inset image, the Ce filler and the Sb atoms are denoted by blue and green filled circles, respectively, and the calculated Sb center by the open circle. In this way, we can provide a simplified solution to evaluate the off-centrosymmetric-position shifts (*i.e.*, shift from the cage center) by using the relative shift between Ce and the calculated Sb position only. The validity of such measurements is also guaranteed by the fact that the calculated center of Sb is found to be coincident with the cage center (see Supporting Information, Note 6). In Figure 3a, the amplitude of the shift vectors can be as large as 60 pm, with the averaged value (*i.e.*, mean) of 18.6 pm and the spread of

shift amplitude (*i.e.*, standard deviation, sd) of 10.0 pm (Figure 3b), further evidencing that the off-center shifts of the Ce filler atoms are prominent.

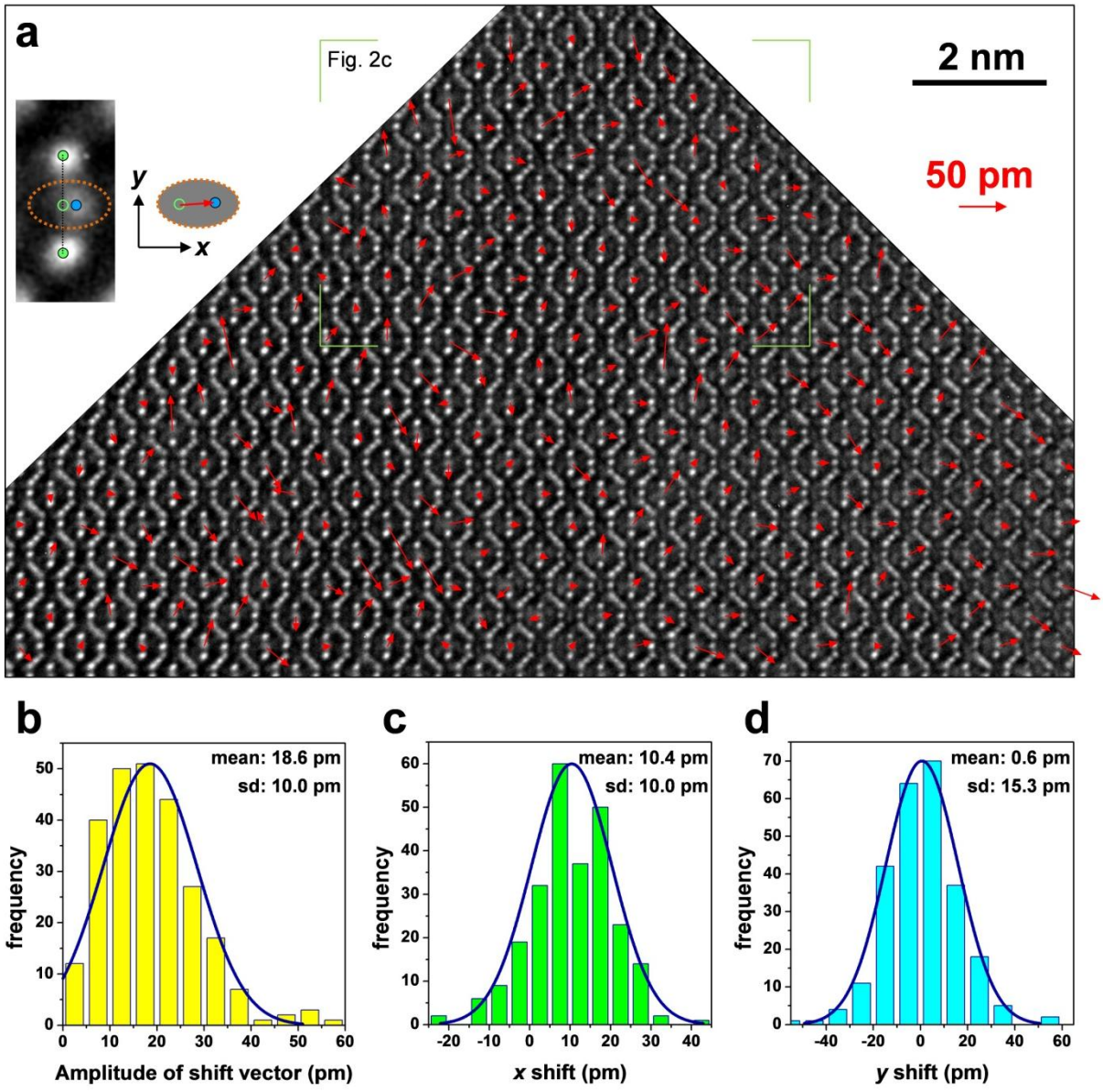

Figure 3. Quantitative measurements of the off-center shifts of the Ce filler atoms in the P-type skutterudite. (a) Vector map of the relative shifts of the Ce atoms with respect to the calculated center of two neighboring Sb, overlaid on the experimental NCSI image. The inset in the left to (a) illustrates how to measure the off-center shift. The arrowhead marks the direction and its length represents the amplitude of the shift. The area marked by the green rectangle is also shown in Figure 2c. (b) Histogram of the amplitude of the Ce shift vectors in (a). (c) and (d) are histograms of the Ce shifts along the ***x*** and ***y*** directions defined in (a), respectively, showing the local directionality of the off-center shifts, *i.e.*, towards +***x*** direction. The effects of imaging imperfections have been removed.

We further plot the histograms of the shift components in the ***x*** and ***y*** direction as shown in Figure 3c and 3d, respectively. It is seen that the averaged value of the Ce atom shifts deviates from the cage center by 10.4 and 0.6 pm, with standard deviations of 10.0 and 15.3 pm in the ***x*** and ***y*** directions, respectively, demonstrating that locally (*i.e.*, within the field of view in Figure 3a) the off-center shifts can have directionality. In addition, it should be mentioned that in comparison with the measurement error of <7 pm, both the average value of measured shifts (Figure 3b) and the measured shift spreads (Figure 3c and 3d) are of statistical significance, confirming the true off-center shifts of the Ce filler atoms in skutterudites.

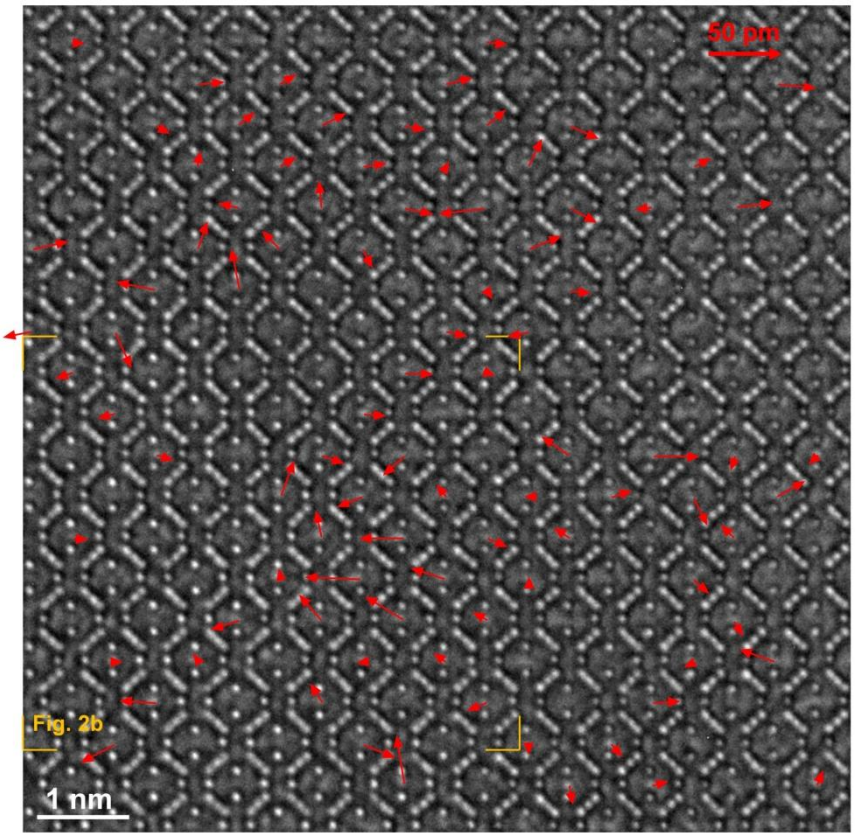

Figure 4. Quantitative measurement of the off-center shifts of the Yb atoms in the N-type skutterudite. (a) Vector map of the relative shifts of the Yb atoms with respect to the calculated center of two neighboring Sb atoms, overlaid on the experimental NCSI image. The area marked by the yellow rectangle is also shown in Figure 2b.

Similarly, we have also measured the off-center shifts of the Yb filler atoms in the N-type sample. Due to the uneven distribution of Yb in the skutterudite lattice, here we chose positions of the Yb atoms in Figure 4 with significant image contrast for quantification. The amplitudes of the shift vectors are measured to be between zero and 37 pm with the mean and

standard deviation values of 15.4 and 7.5 pm, respectively. Meanwhile, the local directionality of the off-center shifts is not observed.

Since in the P-type skutterudite, the filling ratio of Ce is much higher than that of Yb in the N-type sample and the replacement of Co_4 by $CoFe_3$ may also introduce local inhomogeneity in the Co/Fe atom dispersion as well as local charge redistribution, interactions between neighboring fillers and/or interactions with local Fe/Co dispersion could be responsible for the observed directionality of the off-center shifts. Indeed, it has been reported that in the P-type La and Ce filled Fe_4Sb_{12}, quasi-harmonic coupling between the fillers and the host lattice is a dominant factor to the low thermal conductivity.[20] Thus, the observed directionality may be an implication for the breakdown of phonon glass paradigm.

The measurement results are further summarized in Table 1, confirming that the off-center shifts are essentially larger in the P-type sample than that in the N-type sample. This, together with the large filling ratio and the local directionality of shifts, is expected to cause stronger influence on the thermoelectric performance in comparison with the effect of the Yb in the N-type skutterudite.

Table 1. The measured filling ratio, maximal filler shift, amplitude of shift vector, off-center shifts *x* and *y* for the N-type $Yb_{0.2}Co_4Sb_{12}$ and P-type $Ce(CoFe_3)Sb_{12}$ samples. The values in the brackets are stardard deviations.

	Measured filling ratio	Maximal filler shift (pm)	Amplitude of shift vector (pm)	Off-center shift *x* (pm)	Off-center shift *y* (pm)
N-type	17.5%	37 pm	15.4 (7.5)	1.1 (14.4)	1.7 (9.2)
P-type	80%	60 pm	18.6 (10.0)	10.4 (10.0)	0.6 (15.3)

2.3. Rattlers off-centering and lattice thermal conductivity

As demonstrated by our NCSI TEM results, partially-filled N-type $Yb_{0.2}Co_4Sb_{12}$ exhibits considerably lower off-centering of the fillers in comparison with fully-filled P-type $Ce(CoFe_3)Sb_{12}$ sample, as schematically illustrated in Figure 5a. Thermoelectric performance measurements (see Supporting Information, Note 8 for details) reveal that $Ce(CoFe_3)Co_{12}$ has

a much lower lattice thermal conductivity κ_l than $Yb_{0.2}Co_4Sb_{12}$. In order to evaluate the influence of off-centering on phonon scattering, we have conducted a Debye-Callaway model simulation for pure Co_4Sb_{12}, partially-filled $Yb_{0.2}Co_4Sb_{12}$ and fully-filled $Ce(CoFe_3)Co_{12}$.

As stated in the introduction part, the off-center effect can be understood in terms of either lattice strain or phonon spectrum (vibration mode) perturbation. To accommodate the Debye-Callaway model, additional factor that off-center rattling (as compared with on-center rattling) imposes on phonon scattering is hereby concluded to be a lattice strain parameter Γ_S, which represents the lattice distortion due to fillers' deviation from the equilibrium center positions. The (on-center) rattling is evaluated *via* the classic resonant scattering model and the Fe/Co alloying in P-type $Ce(CoFe_3)Co_{12}$ is assumed to introduce mass and strain fluctuations as traditional point defect scattering. The scattering factors considered in the simulation is then outlined as follows: (i) pure Co_4Sb_3: phonon-phonon scattering + grain boundary scattering; (ii) N-type $Yb_{0.2}Co_4Sb_{12}$: phonon-phonon scattering + grain boundary scattering + resonant scattering + strain scattering; (iii) P-type $Ce(CoFe_3)Co_{12}$: phonon-phonon scattering + grain boundary scattering + Fe/Co alloying scattering + resonant scattering + strain scattering (see Supporting Information, Note 9 for details). The final simulated results are shown in Figure 5b.

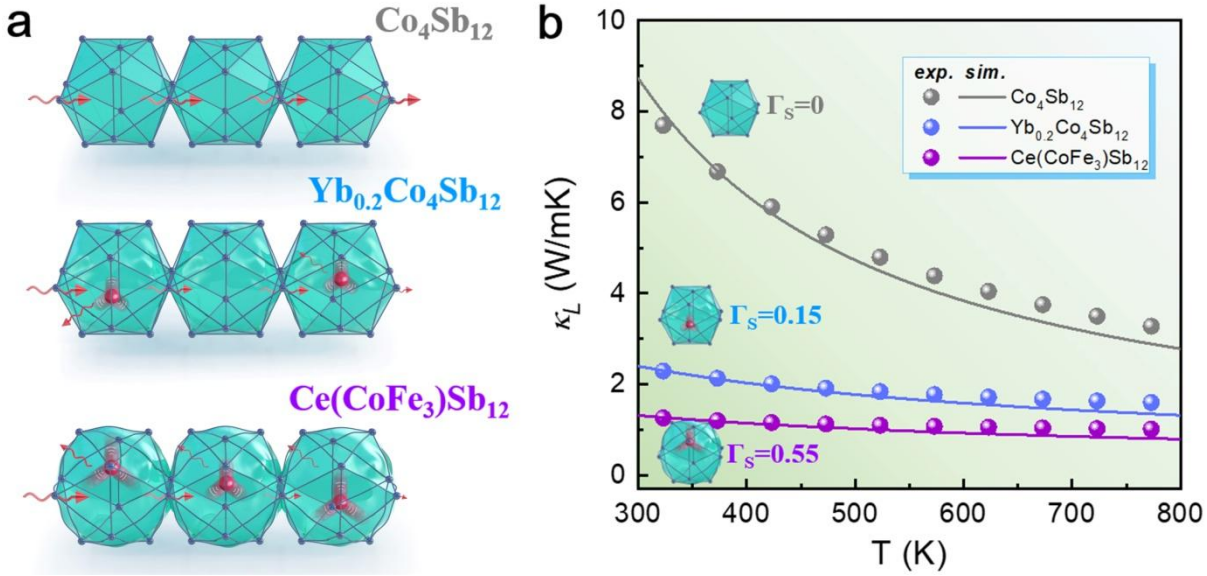

Figure 5. (a) Schematics of lattice strain induced by off-centering rattlers. (b) Lattice thermal conductivity of unfilled Co_4Sb_{12}, Yb partially-filled $Yb_{0.2}Co_4Sb_{12}$ and Ce fully-filled $Ce(CoFe_3)Sb_{12}$ skutterudite samples.

Spectral lattice thermal conductivity simulation (Supporting Information, Note 9) for P-type $Ce(CoFe_3)Co_{12}$ reveals that Fe/Co alloying scattering has minimal effect on phonon scattering due to the very small difference in mass and radius between Fe and Co. It is also shown that resonant scattering dominates at a very localized frequency range only. Direct comparison between N-type $Yb_{0.2}Co_4Sb_{12}$ and P-type $Ce(CoFe_3)Co_{12}$ indicates that: (i) lattice strain due to the off-center feature of Yb/Ce fillers strongly scatters heat-carrying phonons of a broad frequency range, and (ii) the lattice strain ($\Gamma_S \sim 0.55$) in fully-filled $Ce(CoFe_3)Co_{12}$ is considerably larger than that ($\Gamma_S \sim 0.15$) in partially-filled $Yb_{0.2}Co_4Sb_{12}$. Since the parameter Γ_S directly reflects the extent of lattice (icosahedral "cage") distortion induced by off-center fillers, our simulations agree well with the NCSI TEM results that Ce in fully-filled $Ce(CoFe_3)Co_{12}$ exhibits a relatively larger statistic off-center shifts. The fact that off-center rattling (on-center rattling + lattice distortion) could scatter heat-carrying phonons for a much broader frequency range than on-center rattling that only scatter phonons at a localized one thus provides an alternative clue to help understand the ultralow lattice thermal conductivity in filled skutterudites.

3. Conclusion

In summary, using atomic-resolution NCSI TEM, the filler (rattling) atoms in Sb-based skutterudite $(Co,Fe)_4Sb_{12}$, including both 20 at.% partially-filled Yb and fully-filled Ce, are atomically resolved with high contrast in real space. Based on quantitative image simulations, the off-center shifts of filler atoms are unambiguously confirmed and directly measured cage-by-cage with picometer precision. The off-centering of Yb, Ce fillers is believed to cause considerable lattice strain in (Co,Fe)-Sb "cages" and results in a distinct phonon spectrum compared to on-centering fillers based on the evaluation using a modified Debye-Callaway model. Our findings in this work shed light on further evidence for atom off-center shifts in real space for a broad series of material systems.

4. Experimental Section

Materials Synthesis: Co_4Sb_{12} (pure), $Yb_{0.2}Co_4Sb_{12}$ (N-type) and $Ce(CoFe_3)Sb_{12}$ (P-type) skutterudite samples were synthesized by vacuum melting and spark plasma sintering (SPS). The raw materials consisted of high-purity Co (power, 99.99%), Sb (power, 99.99%), Ce (power, 99.99%) and Yb (power, 99.99%). The mixtures were first loaded in double quartz tubes at about 10^{-4} Pa, which could prevent samples from exploding in the tube during cooling

process. Then, the mixtures were heated to 1273 K and maintained for 10 hours. After soaking 10 hours, the tubes were brought to room temperature in 10 hours. The obtained ingots were crushed and ground into powder by high-energy ball milling at 800 rpm for 10 min. The powder was loaded into a φ20 mm graphite die and consolidated using an SPS system (SPS-211Lx, Japan) at 923 K under a pressure of 50 MPa for 5 min.

Phase Structure Characterization: The phase structure of the samples was determined using x-ray diffraction (XRD) on a Bruker D8 diffractometer with monochromated Cu $K_{\alpha 1}$ radiation (wavelength = 1.541 Å). The XRD scan ranges from 10 to 70º with a speed of 10°· min^{-1} and a step size of 0.02°.

Thermoelectric Properties Measurement and Analysis: The electrical conductivity (σ) and Seebeck coefficient (S) of all samples were measured (ZEM-3, ULVAC-RIKO, Japan) in a rarefied helium atmosphere. The thermal diffusivity (D) of all bulk samples were measured by laser flash method (LFA 457, NETZSCH LFA, Germany) in an Ar atmosphere using Cowan model plus pulse correction, and the total thermal conductivity (κ) was calculated on the basis of $\kappa = DC_P\rho$ (C_P: heat capacity and ρ: density). The Archimedes method was used to measure the density ρ. Finally, the experimentally determined uncertainty of the figure of merit ZT value is about 15-20%. The approximated lattice thermal conductivity κ_l and fitting details with Debye-Callaway model can be found in Supporting Information, Note 9.

TEM Sample Preparation: Specimens for transmission electron microscopy investigations were prepared from the as-synthesized bulk polycrystals by standard procedures including cutting, mechanical grinding, dimpling and polishing. The final thinning of the specimens was carried out using 5 kV Ar-ion milling in a GATAN Precision Ion Polishing System II, followed by a cleaning process at 1 kV in order to remove damaged layers that may be introduced during the previous step. Specimens for scanning transmission electron microscopy energy dispersive x-ray spectroscopy (Supporting Information, Note 1) were prepared using focused ion beam milling with Ga ions in an FEI Helios NanoLab 460F1 dual beam system.[39]

Transmission Electron Microscopy: Electron microscopy at atomic resolution was performed using the negative spherical aberration (C_S) imaging technique on an image C_S-corrected FEI Titan 80-300 transmission electron microscope working at an accelerating voltage of 300 kV

and a Rayleigh resolution of 80 pm.[40] The NCSI technique yields strong image contrast that is localized as much as possible on the respective atomic columns, allowing ultra-high precision measurement of atom positions on the basis of computer-based image analysis.[33-35] Residual lens aberrations of the microscope were measured by the Zemlin tableau method and minimized rightly before image acquisition. The images were recorded using a GATAN UltraScan 1000 2k × 2k charge-coupled device camera at a sampling rate of 9 pm per pixel. Atomic-resolution high-angle annular dark-field scanning transmission microscopy imaging and corresponding energy dispersive x-ray spectroscopic (EDXS) elemental mapping displayed in the Supporting Information, Note 1 were carried out at 200 kV in an FEI Titan G^2 80-200 ChemiSTEM microscope equipped with a high-brightness field emission gun, a probe C_S corrector, and a super-X EDXS system.[41] The incident electron beam convergence semi-angle for HAADF STEM imaging was about 25 mrad, while the collection semi-angle was 70-200 mrad. EDXS were collected and analyzed using Bruker ESPRIT and Thermo Scientific Velox software.

Image Simulations and Quantification: Multislice image simulations for both NCSI and HAADF STEM were carried out using Dr. Probe software.[42] Atomic models used in the simulations were modified using home-made scripts on the basis of ICSD-185372[37] and were visualized using VESTA software[43]. Quantitative comparison between experimental and simulated NCSI images was performed on the absolute contrast scale[34,44,45] by taking into account the effect of camera modulation-transfer function, specimen absorption and image spread resulted mainly from thermal magnetic field noise (Johnson noise)[46] in the optical path of a microscope using an iterative and semi-automatic approach with the assistance of home-made software package. Prior to comparison, the mean intensity of each image was normalized to a dimensionless value of 1, and the corresponding standard deviation of intensity spread represented the image contrast.[34] Simulation parameters for the best-fit NCSI images are listed in Supporting Information Table S1.

[Further details of the crystal structure investigation(s) may be obtained from the Fachinformationszentrum Karlsruhe, 76344 Eggenstein-Leopoldshafen (Germany), on quoting the depository number ICSD-185372]

Supporting Information

Supporting Information is available.

Acknowledgements

This work was financially supported by the National Natural Science Foundation of China (Grant No. 52162029), Natural Science Foundation of Shaanxi Province (grant No. 2021JM-201), Academician (Expert) Workstation of Yunnan Province Program (Grant No. 202005AF150010), Yunnan Provincial Natural Science Key Fund (Grant No. 202101AS070015). W.D. thanks the support of Shaanxi Sanqin Scholars Innovation Team. The authors thank Juri Barthel (RWTH Aachen University and Forschungszentrum Jülich GmbH) for sharing the home-made software package for semi-automatic quantitative image comparison.

References

[1] G. A. Slack, in *CRC handbook of thermoelectrics*, (Ed: D. M. Rowe), pp. 407-440, CRC Press LLC, Boca Raton, Florida, USA, **1995**, Ch. 34.

[2] M. Rull-Bravo, A. Moure, J. F. Fernández, M. Martín-González, *RSC Adv.* **2015**, *5*, 41653.

[3] B. C. Sales, D. Mandrus, R. K. Williams, *Science* **1996**, **272**, 1325-1328.

[4] X. Shi, J. Yang, J. R. Salvador, M. Chi, J. Y. Cho, H. Wang, S. Bai, J. Yang, W. Zhang, L. Chen, *J. Am. Chem. Soc.* **2011**, *133*, 7837-7846.

[5] Y. Tang, Z. M. Gibbs, L. A. Agapito, G. Li, H. S. Kim, M. B. Nardelli, S. Curtarolo, G. J. Snyder, *Nature Mater.* **2015**, *14*, 1223-1228.

[6] W. Zhao, Z. Liu, Z. Sun, Q. Zhang, P. Wei, X. Mu, H. Zhou, C. Li, S. Ma, D. He, P. Ji, W. Zhu, X. Nie, X. Su, X. Tang, B. Shen, X. Dong, J. Yang, Y. Liu, J. Shi, *Nature* **2017**, *549*, 247-251.

[7] Y. Z. Pei, L. D. Chen, W. Zhang, X. Shi, S. Q. Bai, X. Y. Zhao, Z. G. Mei, X. Y. Li, *Appl. Phys. Lett.* **2006**, *89*, 221107.

[8] Y. Z. Pei, J. Yang, L. D. Chen, W. Zhang, J. R. Salvador, J. Yang, *Appl. Phys. Lett.* **2009**, *95*, 042101.

[9] D. T. Morelli, G. P. Meisner, B. Chen, S. Hu, C. Uher, *Phys. Rev. B* **1997**, *56*, 7376-7383.

[10] G. S. Nolas, J. L. Cohn, G. A. Slack, *Phys. Rev. B* **1998**, *58*, 164-170.

[11] G. S. Nolas, M. Kaeser, R. T. L. IV, T. M. Tritt, *Appl. Phys. Lett.* **2000**, *77*, 1855-1857.

[12] A. Grytsiv, P. Rogl, S. Berger, C. Paul, E. Bauer, C. Godart, B. Ni, M. M. Abd-Elmeguid, A. Saccone, R. Ferro, D. Kaczorowski, *Phys. Rev. B* **2002**, *66*, 094411.

[13] L. D. Chen, T. Kawahara, X. F. Tang, T. Goto, T. Hirai, J. S. Dyck, W. Chen, C. Uher, *J. Appl. Phys.* **2001**, *90*, 1864-1868.

[14] M. Puyet, B. Lenoir, A. Dauscher, M. Dehmas, C. Stiewe, E. Müller, *J. Appl. Phys.* **2004**, *95*, 4852-4855.

[15] X. Y. Zhao, X. Shi, L. D. Chen, W. Q. Zhang, W. B. Zhang, Y. Z. Pei, *J. Appl. Phys.* **2006**, *99*, 053711.

[16] G. S. Nolas, H. Takizawa, T. Endo, H. Sellinschegg, D. C. Johnson, *Appl. Phys. Lett.* **2000**, *77*, 52-54.

[17] B. C. Sales, B. C. Chakoumakos, D. Mandrus, *Phys. Rev. B* **2000**, *61*, 2475-2481.

[18] G. S. Nolas, J. Yang, H. Takizawa, *Appl. Phys. Lett.* **2004**, *84*, 5210-5212.

[19] T. He, J. Chen, H. D. Rosenfeld, M. A. Subramanian, *Chem. Mater.* **2006**, *18*, 759-762.

[20] M. M. Koza, M. R. Johnson, R. Viennois, H. Mutka, L. Girard, D. Ravot, *Nature Mater.* **2008**, *7*, 805-810.

[21] R. Viennois, L. Girard, D. Ravot, H. Mutka, M. Koza, F. Terki, S. Charar, J. C. Tedenac, *Phys. B* **2004**, *350*, E403-E405.

[22] J. L. Feldman, D. J. Singh, I. I. Mazin, D. Mandrus, B. C. Sales, *Phys. Rev. B* **2000**, *61*, R9209-R9212.

[23] B. C. Chakoumakos, B. C. Sales, D. Mandrus, V. Keppens, *Acta Cryst.* **1999**, *B55*, 341-347.

[24] T. Goto, Y. Nemoto, K. Sakai, T. Yamaguchi, M. Akatsu, T. Yanagisawa, H. Hazama, K.Onuki, H. Sugawara, H. Sato, *Phys. Rev. B* **2004**, *69*, 180511.

[25] F. A. Garcia, D. J. Garcia, M. A. Avila, J. M. Vargas, P. G. Pagliuso, C. Rettori, M. C. G. Passeggi, Jr., S. B. Oseroff, P. Schlottmann, B. Alascio, Z. Fisk, *Phys. Rev. B* **2009**, *80*, 052401.

[26] Y. Fu, X. He, L. Zhang, D. J. Singh, *Phys. Rev. B* **2018**, *97*, 024301.

[27] Y. Qiu, J. Xing, X. Gao, L. Xi, X. Shi, H. Gu, L. Chen, *J. Mater. Chem. A* **2014**, *2*, 10952-10959.

[28] X. Shi, J. Yang, L. Wu, J. R. Salvador, C. Zhang, W. L. Villaire, D. Haddad, J. Yang, Y. Zhu, Q. Li, *Sci. Rep.* **2015**, *5*, 14641.

[29] Y. Wang, J. Mao, Q. Jie, B. Ge, Z. Ren, *Appl. Phys. Lett.* **2017**, *110*, 163901.

[30] Z. Liu, X. Meng, D. Qin, B. Cui, H. Wu, Y. Zhang, S. J. Pennycook, W. Cai, J. Sui, *J. Mater. Chem. C* **2019**, *7*, 13622-13631.

[31] S. J. Pennycook, L. A. Boatner, *Nature* **1988**, *336*, 565-567.

[32] C. L. Jia, M. Lentzen, K. Urban, *Science* **2003**, *299*, 870-873.

[33] C. L. Jia, L. Houben, A. Thust, J. Barthel, *Ultramicroscopy* **2010**, *110*, 500-505.

[34] C. L. Jia, S. B. Mi, J. Barthel, D. W. Wang, R. E. Dunin-Borkowski, K. W. Urban, A. Thust, *Nature Mater.* **2014**, *13*, 1044-1049.

[356] C. L. Jia, L. Jin, Y. H. Chen, K. W. Urban, H. Wang, *Ultramicroscopy* **2018**, *192*, 57-68.

[36] Y. G. Yan, W. Wong-Ng, L. Li, I. Levin, J. A. Kaduk, M. R. Suchomel, X. Sun, G. J. Tan, X. F. Tang, *J. Solid State Chem.* **2014**, *218*, 221-229.

[37] J. L. Mi, M. Christensen, E. Nishibori, B. B. Iversen, *Phys. Rev. B* **2011**, *84*, 064114.

[38] L. Houben, iMtools general purpose multi platform image procession tools, https://er-c.org/index.php/software/stem-data-analysis/imtools/, accessed: 11, **2021**.

[39] Ernst Ruska-Centre for Microscopy and Spectroscopy with Electrons, *J. Large-Scale Res. Facil.* **2016**, *2*, A59. doi: http://dx.doi.org/10.17815/jlsrf-2-105

[40] Ernst Ruska-Centre for Microscopy and Spectroscopy with Electrons, *J. Large-Scale Res. Facil.* **2016**, *2*, A41. doi: http://dx.doi.org/10.17815/jlsrf-2-66

[41] Ernst Ruska-Centre for Microscopy and Spectroscopy with Electrons, *J. Large-Scale Res. Facil.* **2016**, *2*, A43. doi: http://dx.doi.org/10.17815/jlsrf-2-68

[42] J. Barthel, *Ultramicroscopy* **2018**, *193*, 1-11.

[43] K. Momma, F. Izumi, *J. Appl. Crystallography* **2011**, *44*, 1272-1276.

[44] C. L. Jia, J. Barthel, F. Gunkel, R. Dittmann, S. Hoffmann-Eifert, L. Houben, M. Lentzen, A. Thust, *Microsc. Microanal.* **2013**, *19*, 310-318.

[45] L. Jin, J. Barthel, C. L. Jia, K. W. Urban, *Ultramicroscopy* **2017**, *176*, 99-104.

[46] S. Uhlemann, H. Müller, P. Hartel, J. Zach, M. Haider, *Phys. Rev. Lett.* **2013**, *111*, 046101.

Supporting Information

Atomic-scale observation of off-centering rattlers in filled skutterudites

Zhen-Hua Ge, Wen-Jie Li, Jing Feng, Fengshan Zheng, Chun-Lin Jia, Di Wu, and Lei Jin**

Z.-H. Ge, W.-J. Li, J. Feng
Faculty of Materials Science and Engineering, Kunming University of Science and Technology, Kunming 650093, China

F. Zheng, C.-L. Jia, L. Jin
Ernst Ruska-Centre for Microscopy and Spectroscopy with Electrons, Forschungszentrum Jülich GmbH, 52428 Jülich, Germany
E-mail: l.jin@fz-juelich.de

D. Wu
Key Laboratory for Macromolecular Science of Shaanxi Province, Shaanxi Key Laboratory for Advanced Energy Devices, School of Materials Science and Engineering, Shaanxi Normal University, Xi'an 710119, China
E-mail: wud@snnu.edu.cn

Note 1. General information obtained from the <111> projection

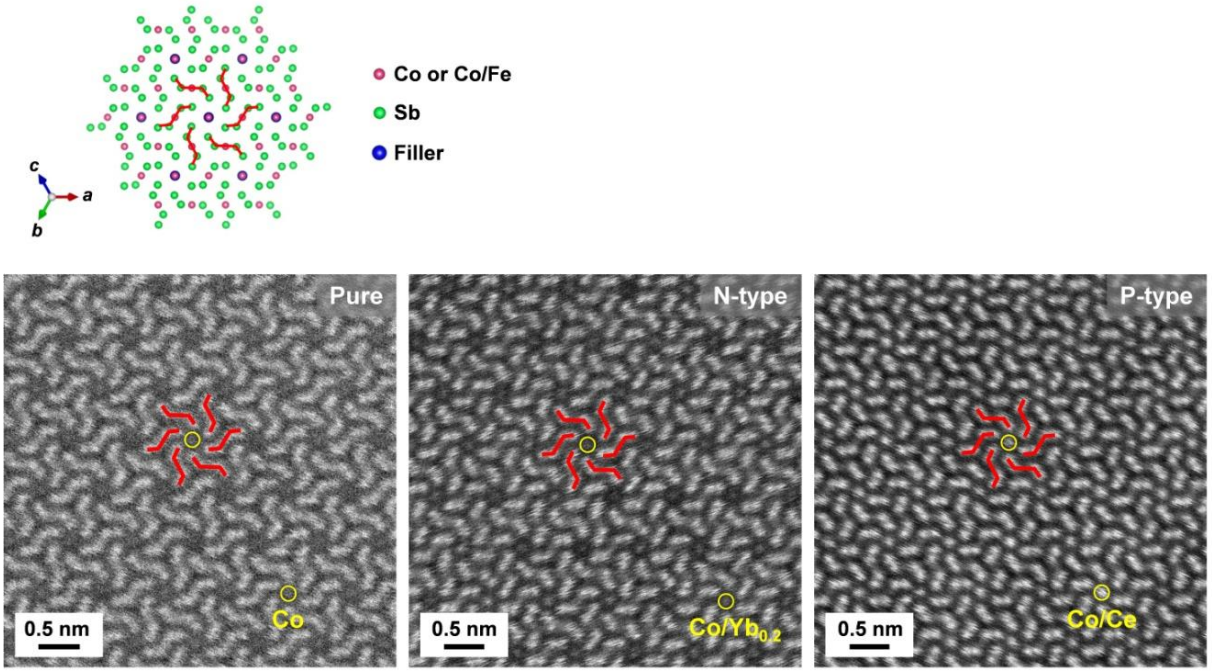

Figure S1. Atomic-resolution high-angle annular dark-field (HAADF) scanning transmission electron microscopy (STEM) images of Co_4Sb_{12} (pure), $Yb_{0.2}Co_4Sb_{12}$ (N-type) and $Ce(CoFe_3)Sb_{12}$ (P-type) recorded along the <111> direction. The transition metal atoms (*i.e.*, Co and Fe) are coincident with the filling atoms along the beam direction, resulting in intrinsic difficulties in quantitative measurements of filling atoms.

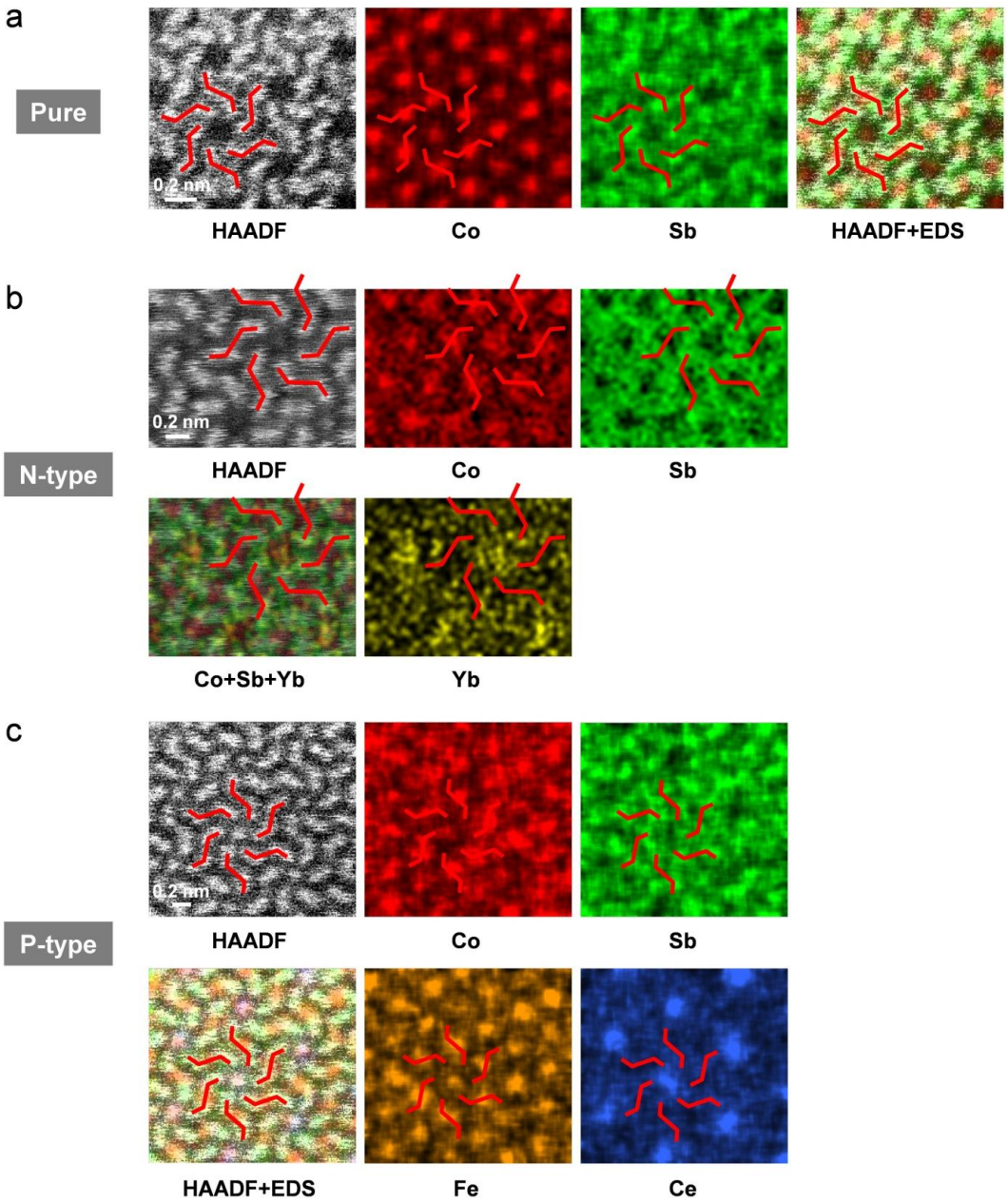

Figure S2. Atomic-resolution HAADF STEM images and corresponding energy dispersive x-ray spectroscopic elemental maps of (a) Co_4Sb_{12} (pure), (b) $Yb_{0.2}Co_4Sb_{12}$ (N-type) and (c) $Ce(CoFe_3)Sb_{12}$ (P-type) recorded along the <111> direction, evidencing the presence of Yb and Ce fillers in skutterudites.

Note 2. Visualization of filler atoms in skutterudites using HAADF STEM

It is well-known that high-angle annular dark-field imaging technique is one of the most popular scanning transmission electron microscopy techniques used in materials research. The

contrast of HAADF STEM is approximately proportional to Z^2 (Z: atomic number), thus it is also called Z-contrast imaging technique.[1]

The HAADF STEM technique has been widely (and even uniquely) used in the studies of skutterudite thermoelectrics, including $Ba_{0.08}La_{0.05}Yb_{0.04}Co_4Sb_{12}$,[2] $Ga_{0.15}Co_4Sb_{11.95}$,[3] $Yb_{0.26}Ga_{0.2}Co_4Sb_{11.9333}$,[4] $Yb_{0.2}Co_4Sb_{12}$,[5] $Yb_{0.28}Co_4Sb_{14.4}$,[6] along the <001> and <111> projections. As mentioned in Supporting Note 1, the filler atoms (usually with relatively low filling ratio) align coincidently with the transition metal atoms (*e.g.*, Co) in the <111> direction, making imaging and quantification intrinsically difficult. In contrast, in the <001> projection (see Figure 1b in the main text) the filler atoms are isolated from neighboring Sb atoms (with a separation of 140 pm between filler and Sb in the projection plane), making quantitative investigation of fillers more feasible.

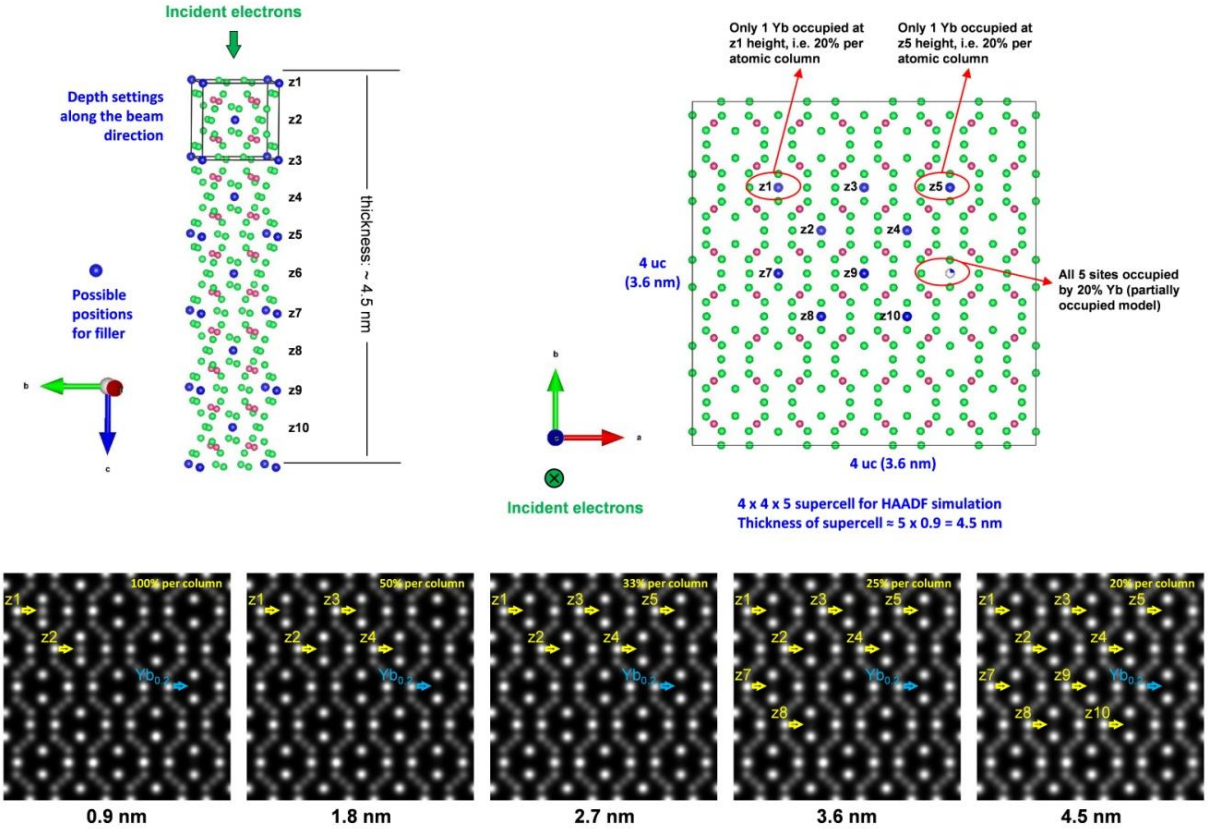

Figure S3. Simulated HAADF STEM images based on a supercell model consisting of locally unfilled (*i.e.*, pure Co_4Sb_{12}) and 20 at.% Yb filled Co_4Sb_{12} sub-regions. The simulation was performed using Dr. Probe software[7] for the experimental ChemiSTEM settings (see Experimental Section in the main text). For simplicity, all aberrations were set to zero.

In order to guide our experiment, we constructed a supercell model consisting of locally unfilled (*i.e.*, pure Co_4Sb_{12}) and 20 at.% Yb filled Co_4Sb_{12} sub-regions for HAADF STEM image simulations. In this model, two filler settings are used: 1) Filler atom site in a column is either fully occupied by Yb or just empty. Since we aim for 20 at.% filling rate, there will be one Yb atom per atomic column (*i.e.*, only one of the five unit cells in the beam direction is occupied by Yb). The depth is denoted by z1…z10. 2) Every filler atom site in the column is partially occupied by 20 % Yb. This is statistically valid especially for relatively thick sample. The results are shown in Supporting Figure S3.

It is obvious that in this extreme case (*i.e.*, filling with light elements or virtually light ones due to low filling rate), the commonly used HAADF STEM imaging of fillers is very challenging, in particular when the thickness is larger than 2.7 nm.

In addition, in the case of quantitative measurement of the off-centering fillers, the residual aberrations of the microscope, the mistilt of the specimen from its ideal Laue zone axis, as well as the scanning distortion, which in practice cannot be fully avoided, are also nontrivial issues.

Therefore, techniques that can image the filler atoms with high spatial resolution and high image contrast are crucial to understand the relation between the thermoelectric performance and the behavior of the filler atoms in skutterudites.

Note 3. Visualization of virtual 100 at.% Li fillers using negative spherical aberration imaging (NCSI)

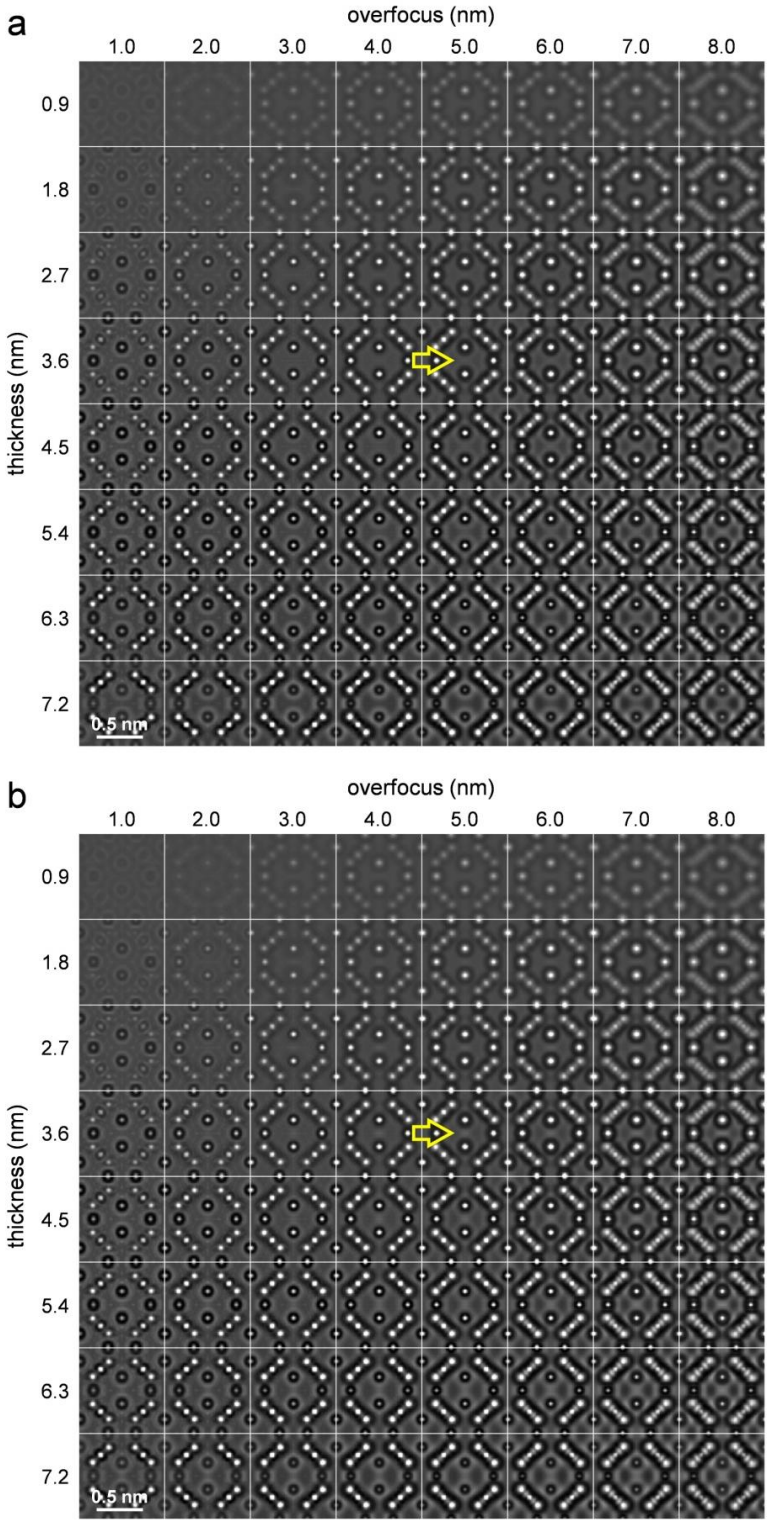

Figure S6. Thickness-focus maps of the simulated images calculated under NCSI condition together with ideal illumination settings for (a) unfilled and (b) virtually 100 at.% Li filled Co_4Sb_{12}. Yellow arrow in (b) marks the position of filler atoms. The similar position is also denoted in (a) for comparison. Simulations were performed using MacTempas software.[8] Practical visibility of super (virtually-) light fillers is then limited by experimental noise resulted from, *e.g.*, uncontrolled surface state of TEM samples.

Note 4. Quantitative image simulations for NCSI

Table S1. Image simulation parameters for NCSI. The azimuth of the simulation parameters is given with respect to the horizontal axis of the image frame in Figure 2. Isotropic *B* parameters for Debye-Waller factors were taken from Reference [9].

Parameter	Co_4Sb_{12}		$Yb_{0.2}Co_4Sb_{12}$		$Ce(CoFe_3)Sb_{12}$	
	Magnitude	Azimuth	Magnitude	Azimuth	Magnitude	Azimuth
Specimen thickness	4.6 nm		3.6 nm		2.4 nm	
Specimen tilt	7.2 mrad	62.7º	4.7 mrad	38.5º	1.9 mrad	306.3º
Absorption	0.27		0.15		0.04	
Image spread	24 pm		22 pm		22 pm	
Focus C_1	+3.9 nm		+5.9 nm		+6.9 nm	
Spherical aberration C_3	–12 µm		–13 µm		–15 µm	
Two-fold astigmatism A_1	1.3 nm	171.3º	0.7 nm	326.3º	0.6 nm	0º
Three-fold astigmatism A_2	112.9 nm	39.6º	52.8 nm	155.4º	74.5 nm	157.9º
Coma B_2	229.6 nm	61.1º	33.1 nm	115.0º	23.3 nm	244.5º
$B_{Co,Fe}$	0.00324 nm^2		0.00324 nm^2		0.00324 nm^2	
B_{Sb}	0.00426 nm^2		0.00426 nm^2		0.00426 nm^2	
B_{Yb}			0.01579 nm^2			
B_{Ce}					0.01421 nm^2	

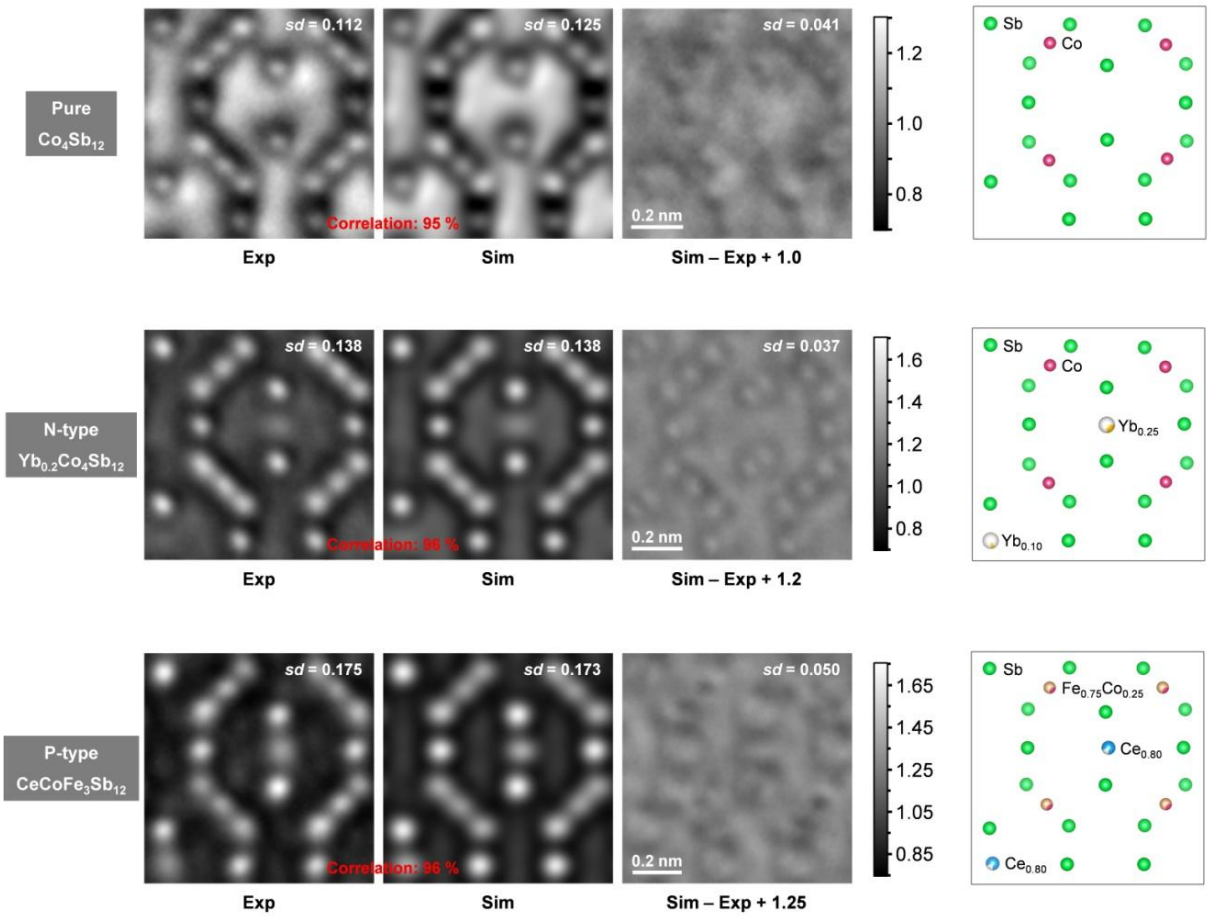

Figure S5. Quantitative comparison between experiment (Exp) and the best-fit simulated image (Sim) at the absolute contrast scale[10-12] for the pure, N-type and P-type samples displayed in Figure 2 in the main text. The atomic models used in the simulation are also given and the simulation parameters are listed in Supporting Table S1. The off-center shift of the filler atoms with respect to the calculated center of two closest Sb neighbors (in the projected plane), see main text for details, are determined and listed below:

N-type $Yb_{0.2}Co_4Sb_{12}$: shift-x = 6.6 pm, shift-y = 0.6 pm, measured from image
shift-x = 0.5 pm, shift-y = 2.3 pm, measured from model

P-type $Ce(CoFe_3)Sb_{12}$: shift-x = 12.9 pm, shift-y = 6.7 pm, measured from image
shift-x = 11.3 pm, shift-y = 2.5 pm, measured from model

The difference in the measured shift values from the image from the corresponding model shows the effect of illumination imperfections, *e.g.*, residual aberrations, specimen mistilt from ideal Laue zone axis, *etc.* Therefore, through image simulations and quantitative comparison, the artifacts coming from the illumination imperfections can be removed.

Note 5. Precision for atom shift measurement from the experimental image

Owing to the superior signal to noise ratio of the images obtained by NCSI technique,[13] the fitting precision of intensity maximum (*i.e.*, atom positions) using two-dimensional Gaussians can reach sub-picometer range, thus it can be considered as a negligible factor in the determination of measurement error.

As described in Section 2.2 in the main text, the measurement error is defined by the root mean square (rms) of atom-site deviations between the experimental and the best-fit periodic lattice of the Co_4Sb_{12} framework. This is demonstrated in Supporting Figure S6a, in which the red dots correspond to the determined position of intensity maxima (corresponding atom positions) of the experimental image and the blue mesh is the best-fit (using least squares method) periodic lattice associated with experiment.

Supporting Figure S6c shows all sub-lattices in a skutterudite unit cell, and Figure S6b illustrates an example for the fit of type A3 sub-lattice.

Supporting Figure S6d to S6g plots the results for all types of sub-lattices in a polar coordinate system for unfilled Co_4Sb_{12}. The measurement error is better than 7 pm in both horizontal (*i.e.*, $\boldsymbol{x}$ direction) and vertical (*i.e.*, $\boldsymbol{y}$ direction) directions. Similar results were obtained from the Co_4Sb_{12} framework for P- and N-type sample, as shown in Supporting Figure S7 and S8, respectively. This measurement error serves as an important criterion (*i.e.*, precision of atom positions) for subsequent analysis for the behavior of filler atoms.

Notably, in the Ce filled $(CoFe_3)Sb_{12}$ sample, the site fluctuation of the Ce fillers has a root mean square of 9.8 and 17.4 pm in the x and y directions (Supporting Figure S7e), respectively, which is of statistical significance as compared with the measurement error of <7 pm, deduced from the skutterudite framework. This reveals the validity of our measurement.

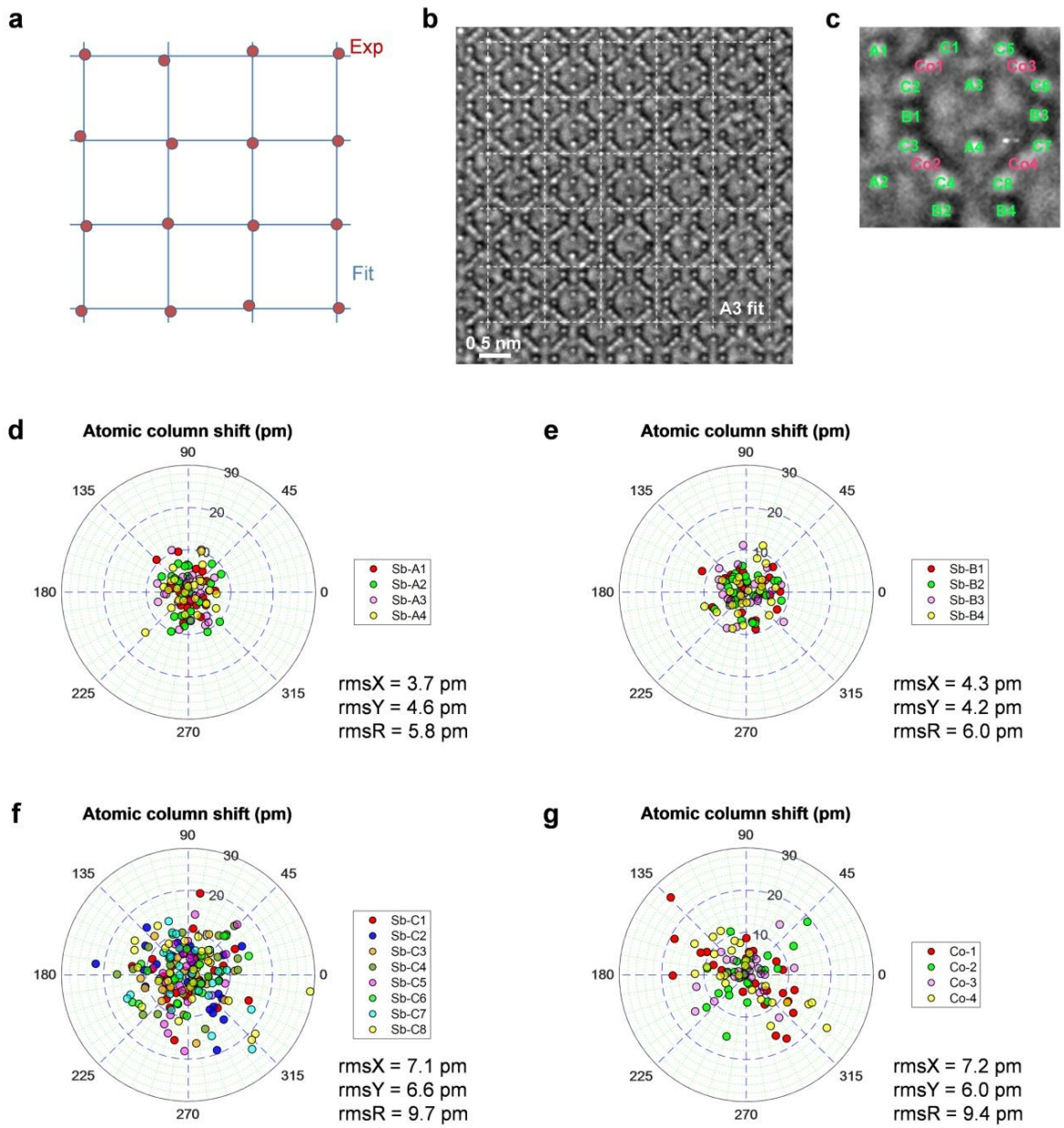

Figure S6. Measurement error for all types of sub-lattices in the unfilled Co_4Sb_{12} sample. (a) Schematics of the sub-lattice fitting using least-squares method. (b) NCSI TEM image illustrating the fitting of A3 sub-lattice. (c) Denotation of different types of sub-lattices in unfilled Co_4Sb_{12}. (d) to (g) Plot of the deviation vectors in a polar coordinate system for A-type Sb, B-type Sb, C-type Sb and Co sub-lattices, respectively. The root mean square for all sub-lattices is <7 pm in both ***x*** and ***y*** directions, which is considered as the precision of atom position measurement.

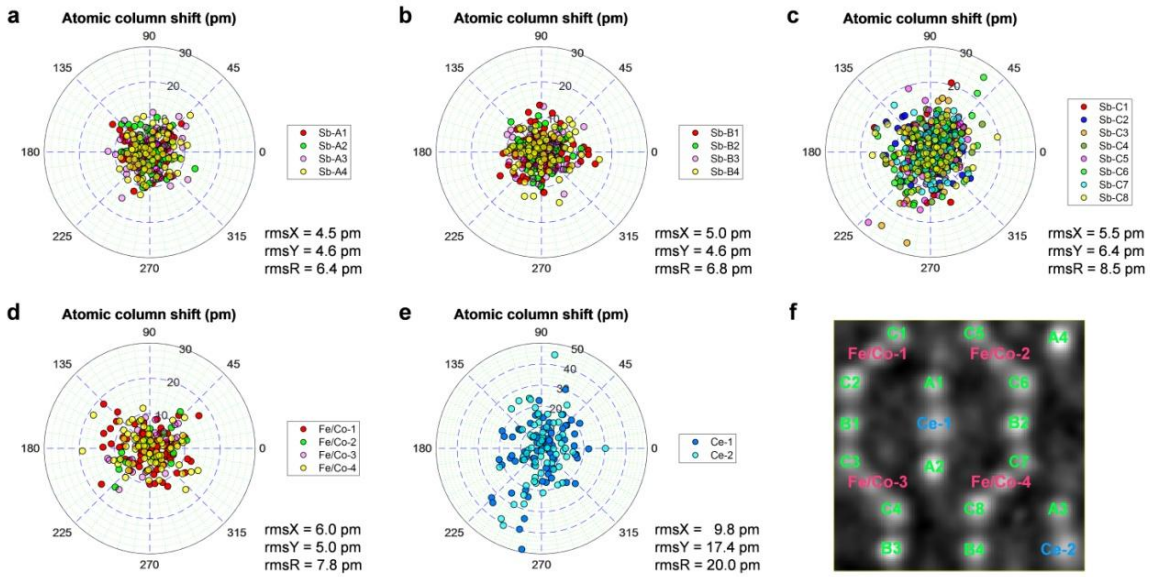

Figure S7. Statistics of the measured shifts for different types of sub-lattices in the Ce filled $(CoFe_3)Sb_{12}$. (a) A-type Sb, (b) B-type Sb, (c) C-type Sb, and (d) Fe/Co sub-lattices. The rms of the measured shifts for all sub-lattices of $(CoFe_3)Sb_{12}$ is <6 pm in both ***x*** and ***y*** directions, which is considered as the error of atom position measurement. (e) For Ce filler, the rms is 9.8 pm and 17.4 pm, evidencing that the position deviation of the Ce filler (from the corresponding best-fit lattice) is statistically significant. (f) Denotation of different types of sub-lattices in the Ce filled $(CoFe_3)Sb_{12}$.

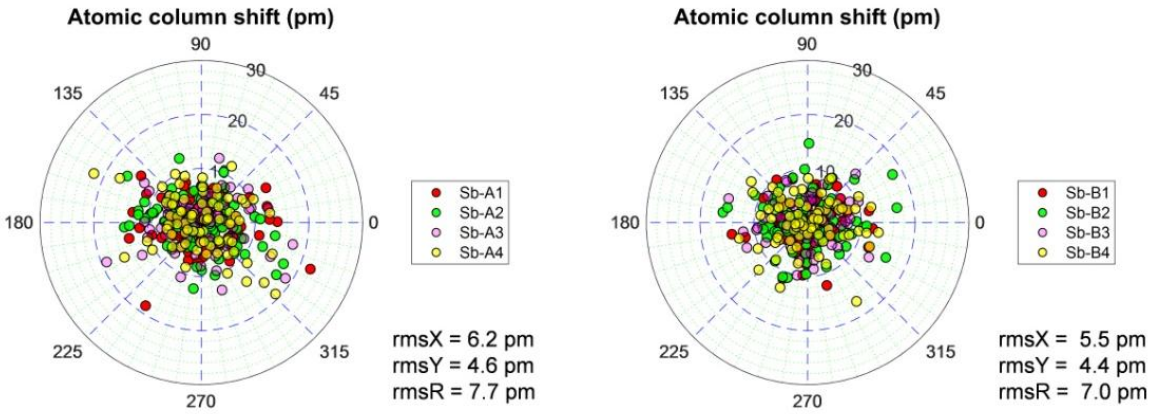

Figure S8. Measurement error (corresponding to rms) evaluated using the A- and B-type Sb sub-lattices in the 20 at.% Yb filled Co_4Sb_{12} sample. Denotation of types of sub-lattice is the same as that in Figure S6.

Moreover, based on the fit as shown Supporting Figure 6a, the lattice parameters for the pure, N-type and P-type samples can be obtained, which are listed in Supporting Table S2. It is found that upon filling, the lattice expands. Meanwhile, the results obtained by NCSI are well comparable with those determined by x-ray diffraction (XRD). In the present work, the lattice parameters are thus re-calibrated on the basis of XRD results, a ratio of 99.3% was applied to the TEM results.

Table S2. Lattice parameters of unfilled Co_4Sb_{12} (pure), $Yb_{0.2}Co_4Sb_{12}$ (N-type) and $Ce(CoFe_3)Sb_{12}$ (P-type) measured by x-ray diffraction (XRD) and transmission electron microscopy (TEM).

	Pure	N-type	P-type
XRD	0.9031 nm	0.9062 nm	0.9105 nm
TEM	0.9077 nm	0.9125 nm	0.9154 nm
TEM × 0.993	0.9013 nm	0.9061 nm	0.9090 nm

Note 6: Determination of the off-center shifts of filler atoms

Practically, there are two simplified methods to determine the off-center shifts of filler atoms:

i) Based on the unit-cell-averaged experimental image, as shown in Figure 1c (or Supporting Figure S5), the (averaged) position of the filler atoms can be determined with respect to the cage center (*i.e.*, the averaged off-centrosymmetric-position shift). For the P-type case, the averaged shift position in the ***x*** and ***y*** direction is 12.9 and 6.7 pm (without simulation correction), respectively. In addition, based on the lattice fit for all individual filler atoms, as demonstrated in Supporting Figure S6a, the root-mean-square (rms) for the position deviations of the filler atoms can be obtained, which is 9.8 and 17.4 pm for Ce in the ***x*** and ***y*** directions (Supporting Figure S7e), respectively. → shift-*x*: 12.9 (*sd* = 9.8) pm; shift-*y*: 6.7 (*sd* = 17.4) pm

ii) The shift of filler atoms can be also measured as the deviation of Ce with respect to the calculated center of the two closest Sb neighbors (in the projected plane). This method is used in the main text. For the P-type case, our results (Figure 3 in the main text) show that the

average shift in the ***x*** and ***y*** direction is 12.0 and 4.8 pm (before simulation correction), with standard deviation (*sd*) of 10.0 and 15.3 pm, respectively. → shift-*x*: 12.0 (*sd* = 10.0) pm; shift-*y*: 4.8 (*sd* = 15.3) pm

It is evident that for the P-type skutterudite, the difference between results that are obtained using method i) and ii) is negligibly small.

In particular, for the N-type case, in which the Yb filler atoms are not evenly distributed in the skutterudite unit cells, *e.g.*, see Figure 2b in the main text, it is more feasible to use method ii) so that both the averaged shifts and related shift spreads (*i.e.*, standard deviation) can be obtained simultaneously.

Note 7: Phase structure of the as-synthesized bulk samples

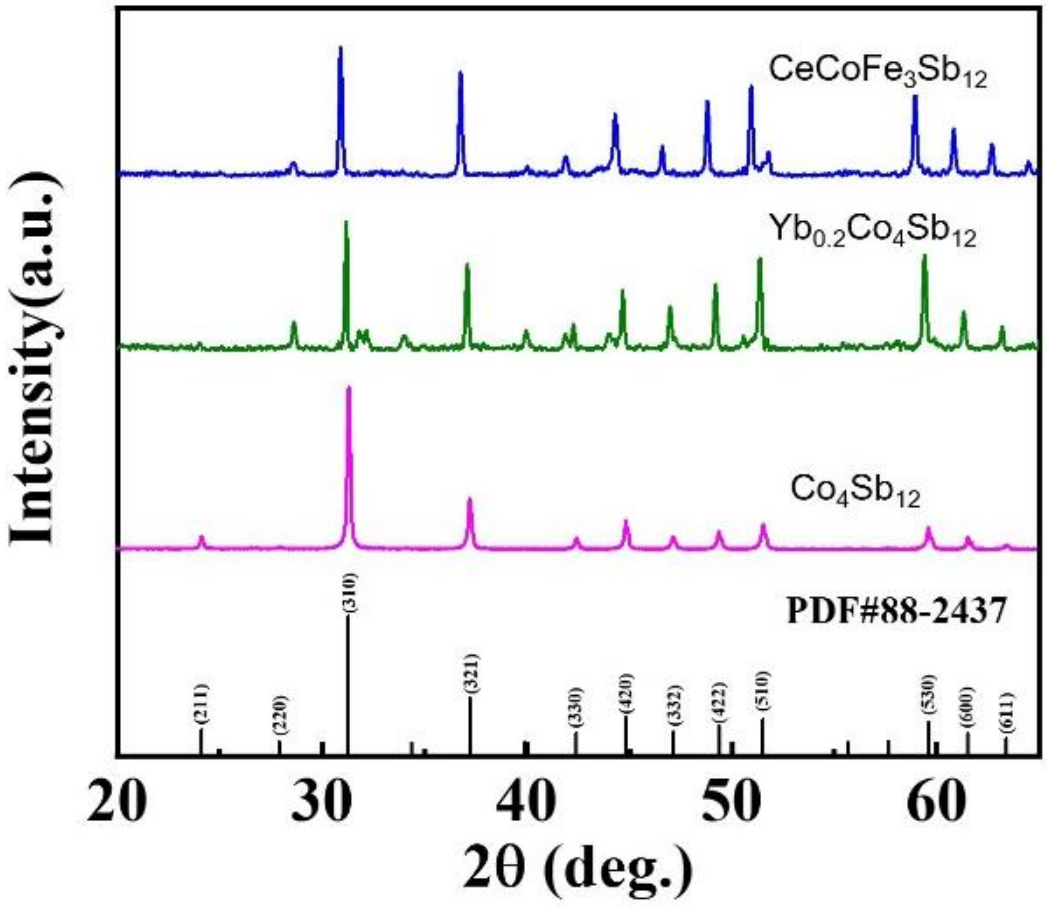

Figure S9. XRD patterns of the as-synthesized bulk samples Co_4Sb_{12} (pure), $Yb_{0.2}Co_4Sb_{12}$ (N-type) and $Ce(CoFe_3)Sb_{12}$ (P-type). Calculated diffractions based on the standard PDF card 88-2437 are displayed as reference.

The phase structure of all synthesized samples was determined by XRD and the results are shown in Supporting Figure S9. Compared with the standard PDF card 88-2437, all samples have a cubic phase. According to the XRD results, the lattice parameter is 0.9031 nm, 0.9062 nm and 0.9105 nm for pure, N- and P-type samples (Supporting Table S2), respectively. It appears that the lattice expands with the increasing of filling rate.

Note 8: Thermoelectric properties of the as-prepared bulk samples

The electrical transport properties, including electrical conductivity σ, Seebeck coefficient S, and thermal transport properties, including thermal diffusivity D and heat capacity C_P of the unfilled Co_4Sb_{12} (pure), $Yb_{0.2}Co_4Sb_{12}$ (N-type) and $Ce(CoFe_3)Sb_{12}$ (P-type) samples were measured at temperatures from 323 to 773 K. The power factor PF and figure of merit ZT value were calculated using the equations: $PF = \sigma S^2$ and $ZT = \sigma S^2 T/\kappa$ (where $\kappa = DC_P\rho$; ρ: density measured by Archimedes method) to evaluate the thermoelectric properties.

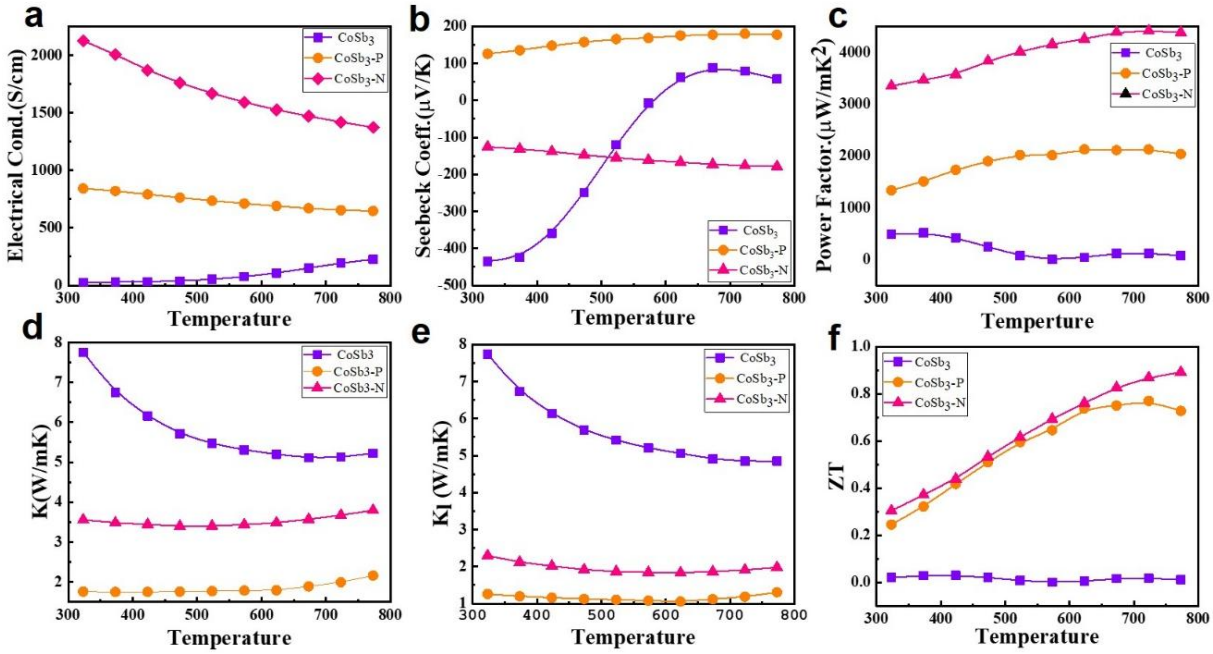

Figure S10. Experimental measurement of thermoelectric performances of pure Co_4Sb_{12} ($CoSb_3$), $Yb_{0.2}Co_4Sb_{12}$ ($CoSb_3$-N) and $Ce(CoFe_3)Sb_{12}$ ($CoSb_3$-P) as a function of absolute temperature T in Kelvin. (a) Electrical conductivity σ, (b) Seebeck coefficient S, (c) Calculated power factor $PF = \sigma S^2$, (d) Total thermal conductivity κ, (e) Lattice thermal conductivity κ_l and (f) Calculated figure of merit ZT value.

Figure S10a shows the temperature dependence of the electrical conductivity of all samples. The pure sample exhibits a semiconductor conductive behavior and has a very low electrical conductivity below 300 Scm^{-1} even at 773 K. When Yb is filled to the lattice of Co_4Sb_{12}, the electrical conductivity is significantly enhanced to 2200 Scm^{-1}. The P-type $Ce(CoFe_3)Sb_{12}$ has a lower electrical conductivity than that of the N-type sample, but the conductivity is still much higher than that of the pure sample. This result is in agreement with the reported data.[14]

The Seebeck coefficients of all samples are shown in Figure S10b. The pure sample exhibits a *p* and *n* turning within the whole measurement temperature range. The N-type sample shows a Seebeck coefficient varying from -100 to -200 μVK^{-1} and the P-type sample has a Seebeck coefficient from 100 to 200 μVK^{-1}. The result further confirms that both N- and P-type Co_4Sb_{12} samples were obtained. Figure S10c shows the calculated power factor (*PF*) value. Due to the highest electrical conductivity and proper Seebeck coefficient, the N-type sample yields the highest *PF* of 4400 $\mu Wm^{-1}K^{-1}$, which is a very high value among all of the thermoelectric materials. The P-type sample possesses a *PF* of 2000 $\mu Wm^{-1}K^{-1}$, which is two magnitudes higher than that of the pure Co_4Sb_{12} sample.

Figure S10d shows the temperature dependence of the thermal conductivity κ for all samples, in which the pure sample has a high thermal conductivity of about 8 $Wm^{-1}K^{-1}$. After introducing filling atoms, the thermal conductivity is decreased to 4 $Wm^{-1}K^{-1}$ in the N-type sample, and further decreased to 1.5 $Wm^{-1}K^{-1}$ for the P-type sample. The lattice thermal conductivity κ_l of all samples is shown in Figure S10e, indicating that the lattice thermal conductivity dominates the total thermal conductivity of Co_4Sb_{12} based thermoelectric materials.

The calculated figure of merit *ZT* value of all the samples are shown in Figure S10f. It is found that the N-type and P-type samples have much higher *ZT* value in the whole measurement temperature range, as compared with the pure sample. This suggests that filled skutterudites are a series of promising thermoelectric materials for application.

Note 9: Debye-Callaway model

(i) *Approximation of experimental lattice thermal conductivity* κ_l

The lattice thermal conductivity κ_l is calculated by subtracting the contribution from carriers (κ_e), and if necessary, the bipolar conduction (κ_{bp}) at high temperatures. In the simplest assumption, κ - κ_e consists of two parts:

$$\kappa-\kappa_e = \frac{A}{T} + B\exp\left(\frac{E_g}{k_B T}\right) \qquad \text{(S1)}$$

where κ and κ_e are total thermal and electron thermal conductivity, respectively. A, B are fitting parameters, E_g, k_B and T are band gap , Boltzmann constant and absolute temperature, respectively. The first term in Equation S1 denotes the contribution from lattice vibration (*i.e.*, κ_l), while the second term represents the contribution of bipolar effects (*i.e.*, κ_{bp}). We took a linear fitting of the lattice part to $1/T$ and obtained approximated lattice thermal conductivity κ_l for samples Co_4Sb_{12} (*i.e.*, $CoSb_3$), N-type $Yb_{0.2}Co_4Sb_{12}$ and P-type $Ce(CoFe_3)Sb_{12}$, as shown in Figure S11.

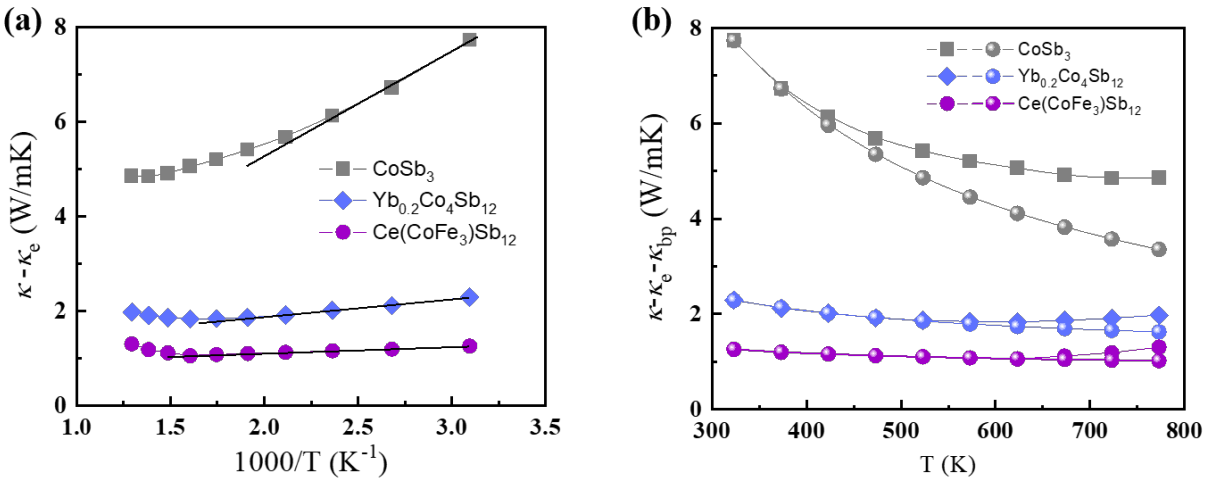

Figure S11. (a) The $1/T$ dependence of κ - κ_e for samples Co_4Sb_{12} (*i.e.*, $CoSb_3$), N-type $Yb_{0.2}Co_4Sb_{12}$ and P-type $Ce(CoFe_3)Sb_{12}$; (b) approximated lattice thermal conductivity κ - κ_e - κ_{bp} (shiny symbols) versus κ - κ_e (matt symbols).

(ii) *Simulation of lattice thermal conductivity*

A modified Debye-Callaway model is used to analyze the individual contribution of phonon scattering mechanism to the overall lattice thermal conductivity. Scattering mechanisms including Umklapp processes (U), Normal processes (N), grain boundary scattering (GB), rattle effect (R) and lattice strain scattering (LS) due to rare earth filling in (Co,Fe)-Sb cages.

We ignore the point defect scattering (mass fluctuation and strain fluctuation) due to Co/Fe substitution in the sample $Ce(CoFe_3)Sb_{12}$, since Fe and Co are neighbors in the periodic table and the difference between their atomic mass and radius is negligibly small. The lattice thermal conductivity κ_l can be expressed as:[15]

$$\kappa_{lat} = \frac{k_B}{2\pi^2 \upsilon}\left(\frac{k_B T}{\hbar}\right)^3 \int_0^{\theta_D/T} \tau_c \frac{x^4 e^x}{(e^x - 1)^2} dx \qquad \text{(S2)}$$

where $\hbar$ is reduced Plank's constant, υ is the average sound velocity (group speed 2700 m/s)[16], θ_D (= 287 K)[16] is the Debye temperature, and x is defined as $\hbar\omega/k_BT$ (ω is the circular frequency), τ_c is the total relaxation time and calculated by the above scattering mechanisms as:

$$\tau_c^{-1} = \tau_U^{-1} + \tau_N^{-1} + \tau_{GB}^{-1} + \tau_R^{-1} + \tau_{LS}^{-1} \qquad \text{(S3)}$$

Their individual contribution to the total relaxation time is listed as follows:

Umklapp process[17]

$$\tau_U^{-1} = \frac{h\gamma^2}{2\pi M \upsilon^2 \theta_D} \varpi^2 T \exp(-\frac{\theta_D}{3T}) \qquad \text{(S4)}$$

Normal process[18]

$$\tau_N^{-1} = \beta \tau_U^{-1} \qquad \text{(S5)}$$

Umklapp and Normal processes describes the intrinsic phonon-lattice interaction during a typical heat transport process. Here M denotes the average mass per atom, γ is the Grüneisen parameter (γ = 0.95 was used in this work)[19]. β = 18 is a fitting constant, which can be derived *via* fitting experimental lattice thermal conductivity for pure Co_4Sb_{12} with simulated one (considering only Umklapp and Normal processes).

Grain boundary scattering[20]

$$\tau_{GB}^{-1} = \frac{\upsilon}{L} \qquad \text{(S6)}$$

Here L represents the average grain size ~1 μm based on our TEM characterization.

Rattle effect[20]

$$\tau_R^{-1} = \frac{C\varpi^2}{(\varpi^2 - \varpi_0^2)^2} \qquad \text{(S7)}$$

Here ϖ_0 = 3.409 THz denotes the resonant frequency of rattle effect, while C = 3.072×10^{33} s^{-3} is a constant. Both parameters were taken from literatures.[20]

Lattice strain of (Co,Fe)-Sb frame induced by rare earth filler (*i.e.*, Yb and Ce)[19,21]

$$\tau_{LS}^{-1} = \frac{4}{17}(\frac{M_B}{M})^2\Gamma \qquad \text{(S8)}$$

Here M_B is the average atomic mass at Co site, Γ is a fitting parameter evaluating the strength of lattice strain.

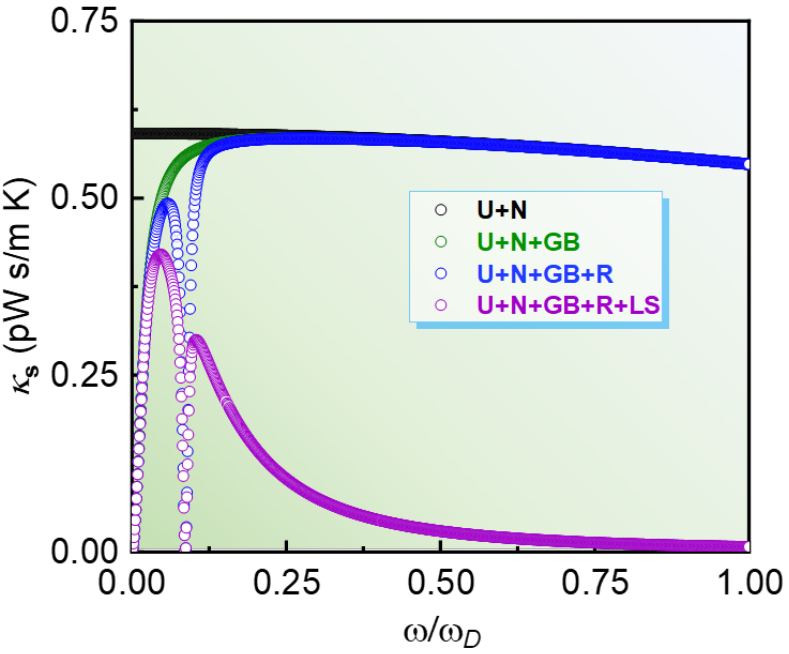

Figure S12. Calculated spectral lattice thermal conductivity κ_s for P-type $Ce(CoFe_3)Sb_{12}$ samples using Debye-Callaway model.

References

[1] S. J. Pennycook, L. A. Boatner, *Nature* **1988**, *336*, 565-567.

[2] X. Shi, J. Yang, J. R. Salvador, M. Chi, J. Y. Cho, H. Wang, S. Bai, J. Yang, W. Zhang, L. Chen, *J. Am. Chem. Soc.* **2011**, *133*, 7837-7846.

[3] Y. Qiu, J. Xing, X. Gao, L. Xi, X. Shi, H. Gu, L. Chen, *J. Mater. Chem. A* **2014**, *2*, 10952-10959.

[4] X. Shi, J. Yang, L. Wu, J. R. Salvador, C. Zhang, W. L. Villaire, D. Haddad, J. Yang, Y. Zhu, Q. Li, *Sci. Rep.* **2015**, *5*, 14641.

[5] Y. Wang, J. Mao, Q. Jie, B. Ge, Z. Ren, *Appl. Phys. Lett.* **2017**, *110*, 163901.

[6] Z. Liu, X. Meng, D. Qin, B. Cui, H. Wu, Y. Zhang, S. J. Pennycook, W. Cai, J. Sui, *J. Mater. Chem. C* **2019**, *7*, 13622-13631.

[7] J. Barthel, *Ultramicroscopy* **2018**, *193*, 1-11.

[8] M. A. O'Keefe, R. Kilaas, *Scanning Microsc.* **1988**, *Suppl. 2*, 225-244.

[9] J. L. Mi, M. Christensen, E. Nishibori, B. B. Iversen, *Phys. Rev. B* **2011**, *84*, 064114.

[10] A. Thust, *Phys. Rev. Lett.* **2009**, *102*, 220801.

[11] C. L. Jia, J. Barthel, F. Gunkel, R. Dittmann, S. Hoffmann-Eifert, L. Houben, M. Lentzen, A. Thust, *Microsc. Microanal.* **2013**, *19*, 310-318.

[12] C. L. Jia, S. B. Mi, J. Barthel, D. W. Wang, R. E. Dunin-Borkowski, K. W. Urban, A. Thust, *Nature Mater.* **2014**, *13*, 1044-1049.

[13] C. L. Jia, L. Houben, A. Thust, J. Barthel, *Ultramicroscopy* **2010**, *110*, 500-505.

[14] Y. Qiu, L. Xi, X. Shi, P. Qiu, W. Zhang, L. Chen, J. R. Salvador, J. Y. Cho, J. Yang, Y. C. Chien, S. W. Chen, Y. Tang, G. J. Snyder, *Adv. Funct. Mater.* **2013**, *23*, 3194-3203.

[15] J. Callaway, *Phys. Rev.* **1959**, *113*, 1046-1051.

[16] D. T. Morelli, T. Caillat, J. P. Fleurial, A. Borshchevsky, J. Vandersande, B. Chen, C. Uher, *Phys. Rev. B* **1995**, *51*, 9622-9628.

[17] D. Morelli, J. Heremans, G. Slack, *Phys. Rev. B*, **2002**, *66*, 195304.

[18] J. He, S. N. Girard, M. G. Kanatzidis, V. P. Dravid, *Adv. Funct. Mater.* **2010**, *20*, 764-772.

[19] G. Meisner, D. Morelli, S. Hu, J. Yang, C. Uher, *Phys. Rev. Lett.* **1998**, *80*, 3551-3554.

[20] G. Nolas, G. Fowler, J. Yang, *J. Appl. Phys.* **2006**, *100*, 043705.

[21] B. Abeles, *Phys. Rev.* **1963**, *131*, 1906-1911.